

Balance of emission and dynamical controls on ozone during KORUS-AQ from multi-constituent satellite data assimilation

K. Miyazaki¹, T. Sekiya¹, D. Fu², K. W. Bowman², S. S. Kulawik³, K. Sudo^{1,4}, T. Walker⁵, Y. Kanaya¹, M. Takigawa¹, K. Ogochi¹, H. Eskes⁶, K. F. Boersma^{6,7}, A. M. Thompson⁸, B. Gaubert⁹, J. Barre¹⁰, and L. K. Emmons⁹

¹Japan Agency for Marine-Earth Science and Technology, Yokohama, Japan

²Jet Propulsion Laboratory, California Institute of Technology, Pasadena, CA, USA

³Bay Area Environmental Research Institute, Sonoma, CA, USA

⁴Graduate School of Environmental Studies, Nagoya University, Nagoya, Japan

⁵Department of Civil and Environmental Engineering, Carleton University, Ottawa, Ontario, Canada

⁶Royal Netherlands Meteorological Institute (KNMI), De Bilt, the Netherlands

⁷Wageningen University, Meteorological and Air Quality department, Wageningen, the Netherlands

⁸NASA/Goddard Space Flight Center, Greenbelt, Maryland, USA

⁹Atmospheric Chemistry Observations & Modeling (ACOM) Laboratory, National Center for Atmospheric Research, Boulder, CO 80307 USA

¹⁰European Centre for Medium-Range Weather Forecasts, Reading, UK

Corresponding author: Kazuyuki Miyazaki (kmiyazaki@jamstec.go.jp)

Key Points:

- Multi-constituent data assimilation during KORUS-AQ showed that emissions in South Korea were 0.42 TgN for NO_x and 1.1 TgCO for CO
- These emissions were 40% and 83% higher, respectively, than the a priori bottom-up inventories, and increased ozone by up to 7.5±1.6 ppbv
- Mean ozone concentration was persistently higher over Seoul (75.1±7.6 ppbv) than the broader KORUS-AQ domain (70.5±9.2 ppbv) at 700 hPa

Abstract

Global multi-constituent concentration and emission fields obtained from the assimilation of the satellite retrievals of ozone, CO, NO₂, HNO₃, and SO₂ from OMI, GOME-2, MOPITT, MLS, and AIRS/OMI are used to understand the processes controlling air pollution during the Korea U.S.-Air Quality (KORUS-AQ) campaign. Estimated emissions in South Korea were 0.42 TgN for NO_x and 1.1 TgCO for CO, which were 40% and 83% higher, respectively, than the a priori bottom-up inventories, and increased mean ozone concentration by up to 7.5±1.6 ppbv. The observed boundary layer ozone exceeded 90 ppbv over Seoul under stagnant phases, whereas it was approximately 60 ppbv during dynamical conditions given equivalent emissions. Chemical reanalysis showed that mean ozone concentration was persistently higher over Seoul (75.10±7.6 ppbv) than the broader KORUS-AQ domain (70.5±9.2 ppbv) at 700 hPa. Large bias reductions (>75%) in the free tropospheric OH show that multiple-species assimilation is critical for balanced tropospheric chemistry analysis and emissions. The assimilation performance was dependent on the particular phase. While the evaluation of data assimilation fields shows an improved agreement with aircraft measurements in ozone (to less than 5 ppbv biases), CO, NO₂, SO₂, PAN, and OH profiles, lower tropospheric ozone analysis error was largest at stagnant conditions, whereas the model errors were mostly removed by data assimilation under dynamic weather conditions. Assimilation of new AIRS/OMI ozone profiles allowed for additional error reductions, especially under dynamic weather conditions. Our results show the important balance of dynamics and emissions both on pollution and the chemical assimilation system performance.

1 Introduction

With rapid economic development, air quality in East Asia has become increasingly important over recent decades (Akimoto, 2003; Liu et al., 2017; van der A et al., 2017). Tropospheric gases such as ozone, nitrogen oxides (NO_x = NO₂ + NO), and carbon monoxide (CO) play an important role in air quality, tropospheric chemistry, and climate. Tropospheric ozone is the third most important greenhouse gas in the atmosphere (Bowman et al., 2013; Myhre et al., 2013; Stevenson et al., 2013); it is formed from the secondary photochemical production of ozone precursors including hydrocarbons or CO in the presence of NO_x, while it is removed by processes such as in-situ chemical loss and deposition to the ground surface. Tropospheric NO_x concentrations are highly variable in both space and time, reflecting its short chemical lifetime in the atmosphere and the heterogeneous distribution of its sources and sinks. NO_x emission sources are important in determining the atmospheric amount and distribution of NO_x and other air pollutants. However, bottom-up inventories from different sources and regions contain large uncertainties, which result from inaccurate emission factors and activity rates for each source category (Castellanos et al., 2014; Vinken et al., 2014; Oikawa et al., 2015).

Satellite-retrieved measurements have great potential for evaluating global and regional distributions of air pollutants, including their emissions. Global tropospheric ozone fields have

66 been retrieved from the Tropospheric Emission Spectrometer (TES; Herman and Kulawik, 2013)
67 and the Infrared Atmospheric Sounding Interferometer (IASI; Clerbaux et al., 2009).
68 Tropospheric NO₂ columns have been measured from the Global Ozone Monitoring Experiment
69 (GOME; Richter and Burrows, 2002), the Scanning Imaging Absorption Spectrometer for
70 Atmospheric Chartography (SCIAMACHY; Bovensmann et al., 1999), GOME-2 (Callies et al.,
71 2000), and the Ozone Monitoring Instrument (OMI; Levelt et al., 2006; Levelt et al., 2018).
72 Carbon monoxide distributions have been retrieved from IASI (George et al., 2009) and from
73 Measurements of Pollution in the Troposphere (MOPITT; Deeter et al., 2017). These satellite
74 measurements have shown rapid changes in air pollutant emissions over Asia, such as increases
75 in NO_x emissions between 2005 and 2010 and a rapid reduction after 2011 in China (Liu et al.,
76 2017; Miyazaki et al., 2017; Qu et al., 2017), decreasing CO emissions from the United States
77 and China between 2001 and 2015 (Jiang et al., 2017), and a rapid SO₂ emission decrease since
78 2007 for China (Wang et al., 2015; Li et al., 2017). These changes in Asia are of importance for
79 air quality and health problems on both regional and global scales (Wang and Hao, 2012;
80 Verstraeten, et al., 2015). The satellite measurements have also been used to validate bottom-up
81 inventories (Kim et al., 2013; Mijling et al., 2013) and study transboundary influences (Lee et
82 al., 2013) over South Korea.

83 Data assimilation techniques have been used to propagate observational information in
84 time and space, from a limited number of observed species to a wide range of chemical
85 components that are physically and chemically consistent within the precision of individual
86 observations (Lahoz and Schneider, 2014; Bocquet et al., 2015). Various studies have
87 demonstrated the capability of data assimilation techniques in the analysis of chemical species in
88 the troposphere and stratosphere (e.g., Parrington et al., 2009; Flemming et al., 2011 2017;
89 Inness et al., 2013; Miyazaki et al., 2012a, 2012b, 2014, 2015, 2017; Gaubert et al., 2016).
90 Miyazaki et al. (2012b) developed a system to simultaneously optimize concentrations and
91 emissions of various species from assimilation of multi-constituent measurements from multiple
92 satellite sensors. Chemical reanalysis using the ensemble Kalman filter (EnKF) has been used to
93 provide comprehensive information on atmospheric composition variability and to elucidate
94 variations in precursor emissions (Miyazaki et al., 2015, 2017a; Ding et al., 2017; Jiang et al.,
95 2018). It has also been used to validate chemistry-climate model simulations (Miyazaki and
96 Bowman, 2017). The chemical reanalysis performance has been evaluated using independent
97 satellite measurements and aircraft measurements for various regions (Miyazaki et al., 2015), but
98 not yet specifically for East Asia because of the lack of intensive validation data. It makes the
99 potential of chemical reanalysis in East Asia unclear for studying the local atmospheric
100 environment and its impacts on the global air quality and climate.

101 During the Korea U.S.-Air Quality (KORUS-AQ) campaign of May–June 2016, aircraft,
102 ground-based, and ozonesonde observations were conducted around the Korean Peninsula by the
103 National Aeronautics and Space Administration (NASA) and the National Institute of
104 Environmental Research (NIER). These measurements provide a great opportunity to evaluate

multiple satellite data assimilation in East Asia. In this study, we use KORUS-AQ measurements to evaluate the performance and efficiency of multi-constituent satellite data assimilation for varying meteorological conditions, and to provide comprehensive tropospheric chemical reanalysis of multi-constituent concentration and emission fields to understand the processes controlling variations in air pollution.

2 Methodology

2.1 Observations during KORUS-AQ

The KORUS-AQ campaign was conducted by NASA and NIER from 1 May to 14 June 2016 over the Korean peninsula. The campaign aimed to implement an integrated observation system for improved understanding of air quality. These observations included three aircrafts (NASA DC-8, NASA B200, Hanseo University King Air), ground in-situ measurements, remote sensing measurements by AERONET, Pandora and LIDAR observations, and several satellite measurements. This campaign has several characteristics. First, Korea's urban/rural sectors are distinct, providing an attractive setting for understanding the relative importance of human and natural emissions. Second, the Korean peninsula and its surrounding waters provide an advantageous experimental setting for distinguishing local and trans-boundary pollution. Third, Korea is located in a region of rapid economic and social change, with strong air quality gradients both in time and space.

We used DC-8 aircraft measurements (23 flights) and ozonesonde measurements over Taehwa (42 profiles, located in a forest area near Seoul) and Olympic Park (20 profiles, located in an urban area of Seoul). Some of the DC-8 flight track information is provided by Tang et al. (2018). 60-second merge R4 data of various species measurements on board DC-8 were used: ozone, NO₂, and NO obtained using 4-channel chemiluminescence instrument (Weinheimer et al., 1993); NO₂ using Thermal-Dissociation Laser Induced Fluorescence (TD-LIF; Thornton et al., 2000); OH and HO₂ concentrations using Laser Induced Fluorescence; OH reactivity with discharge flow (Brune et al., 1995); CO using Differential Absorption Carbon Monoxide Measurements (DACOM; Warner et al., 2010); CH₂O using Compact Atmospheric Multispecies Spectrometer (CAMS; Weibring et al., 2007); PAN and SO₂ using the chemical ionization mass spectrometer (CIMS; Huey et al., 2007); and HNO₃ using single mass analyzer CIMS (S-CIMS; Crounse et al., 2006).

For comparisons with aircraft and ozonesonde observations, all observed profiles were binned on a common pressure grid with an interval of 30 hPa and mapped with a horizontal resolution of 0.5°×0.5°. The reanalysis and model fields were linearly interpolated to the time and location of each measurement using two-hourly output data and then binned on the common pressure grid and horizontal resolution. The validation using DC-8 measurements was conducted both inside and outside the Seoul Metropolitan area (SMA, defined as 36.6°N–37.9°N, 126.4°E–

127.6°E in this study) to discuss the model/data assimilation performance for different chemical regimes.

2.2 Chemical data assimilation system

The data assimilation system used was constructed based on a global CTM and an EnKF. The data assimilation framework is described in Miyazaki et al. (2017); however, some updates have been applied in this study including horizontal resolution (from 2.8°×2.8° to 1.1°×1.1°), assimilated measurements, and data assimilation setting. Here we provide a brief description of the updated data assimilation system.

2.2.1 Forecast model

The forecast model used is MIROC-Chem (Watanabe et al., 2011), which considers detailed photochemistry in the troposphere and stratosphere. The chemistry component of the model, which is based on CHASER-V4.0, calculates the concentrations of 92 chemical species and 262 chemical reactions (58 photolytic, 183 kinetic, and 21 heterogeneous reactions). Its tropospheric chemistry considers the fundamental chemical cycle of O_x–NO_x–HO_x–CH₄–CO along with oxidation of non-methane volatile organic compounds (NMVOCs). Its stratospheric chemistry simulates chlorine and bromine containing compounds, CFCs, HFCs, OCS, N₂O, and the formation of polar stratospheric clouds (PSCs) and heterogeneous reactions on PSC surfaces. More details on the CHASER chemistry module can be found in Morgenstern et al. (2017). In the framework of MIROC-Chem, CHASER is coupled to the atmospheric general circulation model MIROC-AGCM version 4 (Watanabe et al., 2011). The meteorological fields simulated by MIROC-AGCM were nudged toward the six-hourly ERA-Interim (Dee et al., 2011). The emission data used are described in Section 2.3.

The model used has a T106 horizontal resolution (1.1°×1.1°) with 32 vertical levels from the surface to 4.4 hPa. The T106 model has approximately 2.6 times higher horizontal resolution (6.25 times smaller grid cell size) than the model used in our previous data assimilation (T42=2.8°×2.8°). Sekiya et al. (2017) demonstrated that increasing model resolution from T42 to T106 significantly improves the tropospheric NO₂ simulations, with reductions in regional mean model biases (RMSEs) for the annual mean tropospheric NO₂ column by 90% (32%) over eastern China. The increase in model resolution can be expected to improve the representation of spatial variations including those between inside and outside the SMA.

2.2.2 Data assimilation method

Data assimilation was based upon an EnKF approach (Hunt et al., 2007). The EnKF uses an ensemble forecast to estimate the background error covariance matrix and generates an analysis ensemble mean and covariance that satisfy the Kalman filter equations for linear models. In the forecast step, a background ensemble, \mathbf{x}_i^b ($i=1, \dots, k$), is obtained from the evolution

of an ensemble model forecast, where \mathbf{x} represents the model variable, \mathbf{b} is the background state, and k is the ensemble size (i.e., 32 in this study). The background ensemble is converted into the observation space, $\mathbf{y}_i^b = \mathbf{H}(\mathbf{x}_i^b)$, using the observation operator \mathbf{H} , which is composed of a spatial interpolation operator and a satellite retrieval operator. The satellite retrieval operator can be derived from an a priori profile and an averaging kernel of individual measurements (e.g., Eskes and Boersma, 2003; Jones et al., 2003). Using the covariance matrices of observation and background error as estimated from ensemble model forecasts, the data assimilation determines the relative weights given to the observation and the background, and then transforms a background ensemble into an analysis ensemble, \mathbf{x}_i^a ($i=1, \dots, k$). The new background error covariance is obtained from an ensemble forecast with the updated analysis ensemble.

The emission estimation is based on a state augmentation technique. In this approach, background error correlations determine the relationship between the concentrations and emissions of related species for each grid point. The state vector includes surface emissions of NO_x, CO, and SO₂ and lightning NO_x sources, as well as the concentrations of 35 chemical species. Owing to the simultaneous assimilation of multiple-species data and because of the simultaneous optimization of concentrations and emission fields, the global distribution of various reactive gases, including OH, is modified considerably in our system. The changes in various species, especially in OH, propagate the observational information between various species and modulates the chemical lifetimes of many species and improves emission estimates (Miyazaki et al., 2012b, 2015, 2017; Miyazaki and Eskes, 2013). The OMI and GOME-2 NO₂ measurements obtained at different overpass times (c.f., Section 2.2.3) were used to optimize the diurnal NO_x emission variability, following the method of Miyazaki et al. (2017).

Covariance inflation was applied to analyses of both concentrations and emissions to prevent an underestimation of background error covariance and filter divergence caused by sampling errors associated with the limited ensemble size and by model errors, as used in Miyazaki et al. (2015). A constant multiplication inflation factor (8 %) was applied to inflate the forecast error covariance at each analysis step. We also applied conditional covariance inflation to the emission factors to prevent covariance underestimation caused by the application of a persistent forecast model and to maintain emission variability, by inflating the spread to a minimum predefined value (i.e. 30% of the initial standard deviation) at each analysis step. The initial standard deviation was set to be 40% for surface emissions of NO_x, CO, and SO₂. We obtained the optimal value of 40 % from sensitivity experiments, to achieve the best agreements with the assimilated measurements and improve the data assimilation statistics; however, this was done using a 2.8°×2.8° resolution system (Miyazaki et al, 2012b).

To improve data assimilation performance and stability, a covariance localization is applied to neglect the covariance among unrelated or weakly related variables, which has the effect of removing the influence of spurious correlations resulting from the limited ensemble size, as described in Miyazaki et al. (2015). The localization is also applied to avoid the

influence of remote observations that may cause sampling errors, with the cut-off radius of 1643 km for NO_x emissions and 2019 km for CO emissions, lightning sources and chemical concentrations.

Because of the increased horizontal model resolution from 2.8°×2.8° to 1.1°×1.1°, the data assimilation analysis suffers more from errors related to the sampling of the background covariance, due to the increased degrees of freedom in the state vector. Increasing the ensemble size from 32 to 64 in the assimilation improved the performance somewhat. For comparisons we employed 32 members, as was done in the latest decadal chemical reanalysis calculation. Although a strong covariance localization was applied to reduce spurious long-range correlations (c.f., Section 2.2.2), further investigations on the optimal localization length, inflation factor, ensemble size, and other data assimilation settings at different model resolutions would be required.

2.2.3 Assimilated measurements

Assimilated observations were obtained from multiple satellite measurements, as listed below.

- OMI and GOME-2 NO₂

Tropospheric NO₂ column retrievals used were the QA4ECV version 1.1 level 2 (L2) product for OMI (Boersma et al., 2017a) and GOME-2 (Boersma et al., 2017b). Low-quality data were excluded following the recommendations (Boersma et al., 2017c), using the provided quality flag and information on solar zenith angle (<80° were used), cloud radiance fraction (<0.5), and air mass factor (tropospheric air mass factor/geometric air mass factor>0.2). We employed a super-observation approach to produce representative data with a horizontal resolution of the forecast model (1.1°×1.1°) for OMI and GOME-2 observations, following the approach of Miyazaki et al. (2012a). Super observations were generated by averaging all data located within a super-observation grid cell. Super-observation error was estimated using the provided retrieval uncertainty by considering an error correlation of 15 % among the individual satellite observations within a model grid cell and by considering representativeness error. The retrieval uncertainty of individual pixels was calculated based on error propagation in the retrieval, based on uncertainties in level-1 data and subsequent spectral fitting, and contributions from uncertainties in ancillary data (surface albedo, cloud properties) required to calculate the stratospheric NO₂ background and the AMF. Uncertainties in the retrieval a-priori do not play a role because the averaging kernels are used. The detailed error characteristics and validation results of the OMI NO₂ product is described by Boersma et al. (2004, 2018).

- MLS ozone and HNO₃

The Microwave Limb Sounder (MLS) data used were the version 4.2 ozone and HNO₃ L2 products (Livesey et al., 2011). We used MLS data for pressures of less than 215 hPa for ozone and 150 hPa for HNO₃, while excluding tropical-cloud- induced outliers. The provided accuracy and precision of the measurement error were included as the diagonal element of the observation error covariance matrix.

- MOPITT CO

The Measurement of Pollution in the Troposphere (MOPITT) total column CO data used were the version 7 L2 TIR/NIR product (Deeter et al., 2017). The version 7 data generally show smaller retrieval biases and reduced bias variability compared with earlier products, while the TIR-NIR product offers the greatest vertical resolution and the greatest sensitivity to CO in the lower troposphere. The total column averaging kernel was used in the observation operator to estimate simulated total columns. The estimated error, which consists of cumulative error from smoothing error, model parameter error, model error of the radiative transfer model, geophysical noise, and instrumental noise, was used in the observation error. The super-observation approach was also applied to MOPITT observations.

- OMI SO₂

The OMI SO₂ data used were the planetary boundary layer (PBL) vertical column SO₂ L2 product produced with the principal component analysis (PCA) algorithm (Li et al., 2013; Krotkov et al., 2016). The data were produced using a constant air mass factor of 0.36. Only clear-sky OMI SO₂ data (cloud radiance fraction less than 20%) with solar zenith angles less than 70° were used, while the first 10 and last 10 cross-track positions were excluded to limit the across-track pixels, following Fioletov et al. (2016, 2017). Because of the lack of information on observation error in the retrieval data set, the OMI SO₂ error was set to be a constant value of 0.25 DU, which is about half of the standard deviation of the retrieved columns over remote regions (Li et al., 2013).

- AIRS/OMI ozone

We also assimilated observational data from the joint AIRS/OMI version 1 L2 ozone profile product (Fu et al., 2018) in sensitivity data assimilation calculations. The ozone profile retrievals were performed via applying the JPL MUlti-SpEctra, MUlti-SpEcies, Multi-Sensors (MUSES) algorithm to both AIRS and OMI level 1B (L1B) spectral radiances (Fu et al., 2018). The methodology, characteristics and validation of MUSES algorithm have been presented by Fu et al., (2013) for joint TES/OMI ozone retrievals and joint CrIS/TROPOMI carbon monoxide (CO) profiling (Fu et al., 2016), joint TES/MLS CO retrievals (Luo et al., 2013) and AIRS alone methane, HDO, H₂O, and CO retrievals. The AIRS/OMI ozone profile product, containing both global survey (GS) and regional mapping (RE) mode data, are publicly available via Aura Validation Data Center (AVDC) website

(https://avdc.gsfc.nasa.gov/pub/data/satellite/Aura/TES/AIRS_OMI/O3). The GS mode AIRS/OMI data has been produced with a spatial sampling and the retrieval characteristics of ozone profiles equivalent to TES L2 standard data product, demonstrating the feasibility of extending the TES L2 data record via a multiple spectral retrieval approach, while the RE mode processes all available AIRS+OMI measurements over the Korean Peninsula. The GS retrievals show good agreements with WOUDC global ozonesonde measurements, with seasonal and global mean biases of -0.9–14.4 ppbv at 750 hPa, 2.2–5.9 ppbv at 510 hPa, and -7.7–2.9 ppbv at 316 hPa (Fu et al., 2018). The retrieved ozone profile, a priori ozone profile, quality flag, averaging kernels, and the estimated uncertainty matrix for ozone profiles were used in data assimilation.

2.3 Experimental settings

We conducted several data assimilation (i.e., chemical reanalysis) calculations and a model simulation without any assimilation (i.e., control run). The data assimilation and model calculations were started from 1 April 2016, using an initial condition on 1 April obtained from a three-month spin-up model calculation. The comparison of validation results between the assimilation and model simulations were used to measure improvements by data assimilation. In the standard assimilation calculation, none of tropospheric ozone profiles were assimilated. This setting is different from our reanalysis calculation (Miyazaki et al., 2015) because of the lack of TES global survey data during the KORUS-AQ period. To measure the impact of assimilating tropospheric ozone profiles, we conducted sensitivity data assimilation calculations using the AIRS/OMI multispectral tropospheric ozone profile retrievals.

The a priori values for surface emissions of NO_x, CO, and SO₂ were obtained from bottom-up emission inventories. Anthropogenic emissions of NO_x, CO, and SO₂ were obtained from the HTAP version 2 for 2010 (Janssens-Maenhout et al., 2015). The HTAP version 2 data was produced using nationally reported emissions combined with regional scientific inventories from the European Monitoring and Evaluation Programme (EMEP), Environmental Protection Agency (EPA), Greenhouse Gas-Air Pollution Interactions and Synergies (GAINS), and Regional Emission Inventory in Asia (REAS). Emissions from biomass burning were based on the monthly Global Fire Emissions Database (GFED) version 4 (Randerson et al., 2018) for NO_x and CO. Emissions from soils were based on monthly mean of the Global Emissions Inventory Activity (GEIA; Graedel et al., 1993) for NO_x. Volcanic SO₂ emissions were based on results from Andres and Kasgnoc (1998). Lightning NO_x (LNO_x) sources were calculated based on the Price and Rind (1992) scheme. For other compounds, emissions were taken from the HTAP version 2 and GFED version 4 emissions.

Any biases in the assimilated satellite retrievals could degrade the data assimilation performance. However, we did not apply any bias correction to the assimilated measurements because of the difficulty in estimating the bias structure.

3 Evaluation results

3.1 Ozone

3.1.1 Mean profiles

Figure 1 compares the mean vertical ozone profiles from the model simulation without any data assimilation, the chemical reanalysis, independent observations from DC-8 aircraft measurements, and the ozonesonde measurements over Taehwa and Olympic Park averaged over the KORUS-AQ period. The aircraft profiles were averaged over and outside of the SMA. The model generally underestimated mean ozone concentrations throughout the troposphere, except for the ozonesonde measurements over Olympic Park in the lower troposphere. The negative model bias in the lower troposphere is 5–10 ppbv over SMA and 10–16 ppbv over the area outside of the SMA relative to the DC-8 profiles, and 2–11 ppbv over Taehwa. The positive model bias over Olympic Park in the lower troposphere can be attributed to large disagreements between the observed low concentration (38–44 ppbv) and simulated high concentration (approximately 80 ppbv) for specific two flights on 2 and 5 June. In the free troposphere, the model shows a mean negative bias of 2–13 ppbv relative to the DC-8 profiles and up to 17 ppbv relative to the Taehwa ozonesonde profiles. Compared with biases against other measurements, the model bias is smaller for the Olympic park ozonesonde profiles (by up to 8 ppbv) at most altitudes of the free troposphere.

Data assimilation largely reduced the mean model bias in the free troposphere to less than 5 ppbv over SMA and 3 ppbv outside of the SMA relative to the DC-8 measurements, with a bias reduction of larger than 50% over SMA and 60% outside of the SMA. The mean bias became less than 4 ppbv after data assimilation over Taehwa in the free troposphere. Over Olympic Park, data assimilation led to positive biases of 2–10 ppbv in the free troposphere. Note that, when excluding the 2 June Olympic Park ozonesonde profile (when the observed concentrations were anomalously low: 44–66 ppbv below 800 hPa and 74–93 ppbv between 420 and 300 hPa, which are about 35% lower near the surface and 17–30% lower between 950 and 750 hPa than the mean observed concentrations averaged during the campaign over Olympic Park, with numerous erroneous data near the surface), the positive bias was greatly reduced. Compared with the aircraft measurements, the root-mean-square-error (RMSE) was also reduced by 6–45% over SMA and 13–37% outside of the SMA in the free troposphere. In the lower troposphere, the model negative bias was reduced by approximately 70% over SMA and 45% outside of the SMA relative to the DC-8 measurements and became nearly zero over Taehwa, whereas the RMSE was reduced by 10%–20% over SMA and 10%–27% outside of the SMA. The remaining large RMSE values are associated with the occurrence of filament structures in the observed individual profiles. The model vertical profiles appear to be insufficient to resolve

these structures, while the assimilated measurements do not contain sufficient information to constrain this fine-scale variability.

The remaining negative bias in the lower troposphere could be associated with underestimated ozone production by precursors. Assimilating additional observations could be required to further improve the near surface ozone analysis. Spatial gradients in urban chemistry are difficult to capture with a global analysis. For example, Na et al. (2005) suggested that near surface ozone is strongly VOC-limited over the SMA. VOC emission optimization through assimilation of formaldehyde measurements (e.g., Millet et al., 2008) in combination with NO_x and ozone data assimilation could be important. Meanwhile, the representation of meteorological fields and chemical losses need to be carefully evaluated using observations. The simulated meteorological fields were nudged toward the meteorological reanalysis fields (i.e., ERA-Interim) and should realistically represent the actual weather patterns. Nevertheless, the GCM performance could substantially influence the representation of detailed meteorological fields, e.g., in boundary layer height and cloud distribution, which could degrade the chemical data assimilation performance. The spatial representativeness gaps between the measurements and model (at 1.1°×1.1° resolution) could also contribute to the disagreement over the SMA.

Figure 2 compares the spatial distributions of mean ozone concentration from the DC-8 measurements averaged over the campaign period. From the surface to 800 hPa, the observed mean concentrations were high (110–130 ppbv) over the Yellow Sea and were lowest over western Japan (approximately 45 ppbv). The observed concentrations over the Korean Peninsula varied from 72 ppbv to 85 ppbv, with enhancements around Seoul and Busan (80–85 ppbv). Between 800 and 500 hPa, the observed concentrations were high around the west coast of the peninsula (85–90 ppbv) and around Busan (90–100 ppbv). Between 500 and 100 hPa, the observed mean concentrations reached 80–110 ppbv, with relatively high concentrations around Seoul and western Japan.

The model underestimated the regional mean concentration by approximately 14 ppbv between the surface and 800 hPa, 10 ppbv between 800 and 500 hPa, and 16 ppbv between 500 and 100 hPa. The negative model biases were large over the Yellow Sea and the vicinity of the western coast in the lower troposphere (by up to 55 ppbv). The KORUS-AQ measurements over the Yellow Sea were designed to observe strong (sharp) transport of pollution plumes from China, whereas even at the improved T106, the horizontal model resolution is still considered too coarse to simulate the plume structure. Tang et al. (2018) noted that during the 25 May 2016 flight, even forecasts using a grid spacing of 9 by 9 km were not able to capture the transport of enhanced CO and CO₂ over the Yellow Sea, although the impact of using high resolution models for simulating the high ozone plume is not clear. Based on model calculations using the optimized emission (c.f., Section 5), we confirmed that rapid transport of polluted air from China through NO_x emissions resulted in large enhancements of lower tropospheric ozone (30–50 ppbv) over the Yellow Sea during the period (Fig. 3). Thus, model errors in local photochemical

production, precursor emissions in China, and transport processes at both synoptic and finer scales, in addition to the coarse horizontal and vertical resolution of the model, could all contribute to the large underestimation over the Yellow Sea. Also note that the assimilated measurements contain limited information to constrain lower tropospheric ozone over the remote areas. Over the Korean peninsula, the model negative bias was maximized around Busan between 800 hPa and 500 hPa, because of local sources such as industries and power plants emissions.

Data assimilation largely reduced the model bias over the entire Korean peninsula throughout the troposphere and over the oceans, except over the Yellow sea below 800 hPa where most of the negative model bias remained. The regional mean model bias was reduced by 64% between the surface and 800 hPa (to 6 ppbv), 86% between 800 and 500 hPa (to 1.5 ppbv), and 96% between 500 and 100 hPa (to 0.9 ppbv).

3.1.2 Temporal variations

Meteorological conditions varied significantly during the campaign. We divided the period into four phases based on dominant circulation patterns. Because the spatial coverage of the DC-8 measurements is limited and changed largely with time during the campaign, regional ozone distributions over East Asia for each phase cannot be obtained from the DC-8 measurements. We thus used the chemical reanalysis to characterize the regional ozone distributions for all phases. Figure 4 shows the spatial distribution of ozone and horizontal wind in the lower troposphere (at 700 hPa) from the chemical reanalysis for each phase. During phase 1 (1–16 May), when the synoptic weather system dynamically changed, the spatial and temporal variation of mean ozone concentration was weak. In phase 2 (17–22 May), when synoptic flow was weak, stagnant conditions led to strong enhancements of pollution over the Korean Peninsula. In phase 3 (25–31 May), when strong westerlies existed, polluted air was rapidly transported from China to Korea, causing extreme pollution (>78 ppbv) and bad visibility in South Korea. In phase 4 (1–6 June), a blocking pattern determined the large-scale ozone distribution over East Asia, leading to high ozone concentrations over the northern part of the Korean peninsula (>74 ppbv) and northern China (>77 ppbv).

Figure 5 compares the mean vertical ozone profiles from the DC-8 for individual phases, averaged for six flights in phases 1, four flights in phase 2, four flights in phase 3, and three flights in phase 4. In phase 1, the observed concentration increased with height over the SMA, with a minimum concentration of approximately 60 ppbv near the surface. The vertical variation was small outside of the SMA. The observed mean concentration in the boundary layer exceeded 90 ppbv in phases 2 and 3, whereas the mean concentration was almost constant in the free troposphere (75–85 ppbv). In phase 4, the observed concentration decreased from the surface (85–90 ppbv) to the middle troposphere (65 ppbv over the SMA and 75 ppbv outside of the SMA), with a sharp minimum around 600 hPa over the SMA.

The negative model bias in the lower troposphere was large during phases 2–4 (10–18 ppbv over the SMA and up to 20 ppbv outside of the SMA), whereas it was less than 10 ppbv during phase 1 both over and outside of the SMA. The model bias in the free troposphere was largest during phase 2 both over and outside of the SMA (10–23 ppbv), while it was less than 8 ppbv above 700 hPa during phase 4 over the SMA.

Data assimilation largely reduced the model bias in the free troposphere throughout the campaign, whereas the data assimilation efficiency varied largely in the lower troposphere. Most of the lower tropospheric bias remained in phases 2 and 3 especially over the SMA. During these phases under stagnant and transboundary transport conditions, model errors in, for instance, local photochemical processes, precursor's emissions, and boundary layer mixing could prevent improvements in the current data assimilation framework. In contrast, during phases 1 and 4, when observed concentrations over the Korea peninsula were controlled by large scale variations, observational information was propagated efficiently in time and space, improving the data assimilation performance from the surface to the free troposphere. These results highlight that both model performance and data assimilation efficiency are strongly sensitive to meteorological conditions, even at same location and in the same season. Note that the choice of model resolution could influence the dependence of data assimilation efficiency on meteorological conditions.

3.1.3 Evaluation of regional ozone using reanalysis

Data assimilation analysis provides comprehensive information on the spatial and temporal variations in global ozone, which can be used to measure the representativeness of the DC-8 aircraft observations. As summarized in Table 1, at 700 hPa over the SMA, the mean concentration averaged over the campaign period, according to chemical reanalysis, is 76.7 ± 9.4 ppbv with the DC-8 aircraft sampling; this value is comparable to the value observed in complete temporal and spatial sampling over the SMA (75.1 ± 7.6 ppbv). The good agreement between the two samplings demonstrates that the aircraft observations are representative of means over the SMA. The standard deviation is largest for dynamic weather conditions (in phase 1) and it is reduced by approximately 60 % in complete sampling.

In the KORUS-AQ domain, the mean ozone concentration obtained by aircraft sampling is 75.8 ± 5.3 ppbv, which is approximately 5 ppbv higher than the average of the surrounding area (defined as 31.5°N – 37.5°N , 123°E – 132°E , corresponding to the area shown in Fig. 2) in complete sampling (70.5 ± 9.2 ppbv), because the DC-8 aircraft flew mainly over highly polluted areas over the Korean peninsula. The difference in mean ozone concentration between the two samplings (6 ppb) as well as the standard deviation in complete sampling (8.7 ppb) are largest in phase 3 owing to strong latitudinal gradients of ozone associated with the rapid transport of polluted air from eastern China centered over northern South Korea. The difference between the two samplings at 900 hPa (not shown in the table) is 8 ppbv at the mean concentration of the

campaign (77.1 ± 12.2 ppbv in aircraft sampling and 69.1 ± 10.5 ppbv in complete sampling), with large differences in phases 2–4 (7–11 ppbv).

Temporal variation is also different between the two samplings for both the SMA and the KORUS-AQ domain. From phase 3 to 4, the mean ozone level decreased in aircraft sampling by approximately 2 ppbv, whereas it increased in complete sampling by 2.4 ppbv. These differences reveal that the aircraft measurements have limitations in representing the evolution of mean ozone fields associated with changes in meteorological conditions at both local and regional scales.

The mean concentration of ozone over the East Asia domain (defined as 29°N – 45°N , 110°E – 132°E , corresponding to the area shown in Fig. 4) in the complete sampling is 70.2 ± 9.3 ppbv (averaged over the campaign period), which is up to approximately 7 ppbv lower (in phase 3) than that based on aircraft sampling. These results demonstrate that the DC-8 measurements are not representative of monthly and regional means either over the KORUS-AQ domain or over East Asia.

Discrepancies can occur between the estimates using actual aircraft data and the analysis fields because of the coarse model resolution. The standard deviation estimated along the DC-8 flight tracks for each bin (with an interval of 30 hPa) was 20–90% larger in the actual aircraft data than in the data assimilation analysis, showing that the analysis represents only parts of the observed variability. Despite the large differences in the variability, we expect the mean concentrations to be similar because of the large number of aircraft samples over a wide area, except near the surface. Near the surface, evaluations using high resolution model/data assimilation fields would provide more useful estimates.

3.1.4 Analysis uncertainty

Important information regarding data assimilation performance is provided by the error covariance. Analysis spread is estimated as the standard deviation across the ensemble simulations, and it can be regarded as uncertainty of the analysis fields. It is caused by errors in the model input data, model processes, and errors in the assimilated measurements, and it is reduced if the analysis converges to a true state (e.g., Houtekamer and Mitchell, 2005; Houtekamer and Zhang, 2016).

The analysis spread showed distinct variations in both time and space (Fig. 6). In phase 1, the analysis spread was relatively small (< 4 ppbv) over central and southern China, because of eastward transport of air with small spread from the central Eurasian continent. In phase 2, the spread was small within the anticyclone over northeastern China and Korean Peninsula. Within the high-pressure system, more observations are available due to the lack of clouds, and observational information can be accumulated effectively, with reduced influence of polluted air from China, which generally has a larger forecast spread. As a result, the analysis spread over the

SMA was decreased by approximately 30% from the phases 1 (3.8 ppbv) to 2 (2.8 ppbv). In phase 3, when polluted air was transported from China, the analysis spread over the SMA increased again to approximately 4.1 ppbv. In phase 4, both the analysis concentration and its spread increased over central China, whereas the spread over the Korean peninsula decreased to approximately 3.3 ppbv.

The changes in the analysis spread suggest that the impact of data assimilation on the analysis, especially for direct ozone assimilation, will be sensitive to meteorological conditions. The small spread could lead to a small increment from ozone assimilation in phase 2. This suggests that accurate and dense observations of precursors could be more important than ozone measurements to improve ozone analysis for stagnant conditions. In contrast, phase 1 saw dynamic weather conditions (i.e., dynamically-varying weather conditions) and a relatively large spread over a wide area in East Asia; as a result, both local and remote measurements of ozone and precursors can be expected to be important to improve the regional ozone distribution.

Overall, the analysis spread was smaller than the actual analysis and observation difference, with the largest discrepancy in phase 2 when the analysis spread was smallest (as described above) and the analysis-observation difference was large (c.f., Section 3.1.2). The mean value and standard deviation of the actual OmF evaluated using the DC-8 measurements in the lower troposphere (between 860 and 700 hPa) in May 2016 were 6.1 ± 4.5 ppb, in contrast with the estimated analysis spread of 3.9 ± 1.1 ppb. The small analysis spread could reflect the lack of effective observations for measuring analysis uncertainties and the stiff chemical system. The ozone analysis spread in the lower and middle troposphere was sensitive to the spread in surface NO_x emissions when excluding direct ozone assimilation. These results indicate the need for additional observational information and/or stronger covariance inflation for forecasting error covariance and measuring analysis spread corresponding to actual analysis uncertainty. Note that the obtained ozone analysis spread was affected by the choice of inflation factor for NO_x emissions to some extent (c.f., Sec. 2.2.2). The applied inflation factor was chosen to obtain the best agreement with the observed profiles of NO₂ and ozone.

3.2 Various reactive gases

Figure 7 compares the mean vertical profiles of various reactive gases observed from DC-8 measurements averaged during the campaign over and outside of the SMA. The observed mean boundary layer NO₂ concentration is approximately 12 ppbv over the SMA and 1.6 ppbv outside of the SMA. The model underestimates NO₂ by 65% over the SMA and 40% outside of the SMA. Data assimilation mostly removes the model negative bias and reproduced the observed NO₂ profile throughout the troposphere outside of the SMA, whereas the improvement was small over the SMA. The remaining negative bias over the SMA suggests that model processes, such as the diurnal cycle, boundary layer mixing and venting, the chemical lifetime of NO_x, and the chemical equilibrium state, may not be described well over the polluted area.

Meanwhile, the model resolution is not sufficient to resolve local enhancements of NO₂ in such a small area. NO is underestimated by 88% over the SMA and by 70% outside of the SMA within the boundary layer by the model. Data assimilation reduced approximately 20% of the model negative bias outside of the SMA. The remaining NO error both over and outside of the SMA indicates a requirement to improve the NO_x chemistry to better proportion of NO and NO₂

The model underestimates CO by up to 120 ppbv over the SMA and 70 ppbv outside of the SMA below approximately 800 hPa (Fig. 7), as commonly reported in the Copernicus Atmosphere Monitoring Service (CAMS) analysis for the same campaign (Tang et al., 2018) and in other global CTMs (e.g., Stroe et al., 2016). This may reflect underestimated emissions and too short chemical lifetime of CO. Data assimilation removes most of the negative CO bias both over and outside of the SMA, because of the increased surface CO emissions (c.f., Sec. 4).

The model largely overestimates SO₂ below approximately 600 hPa by a factor of up to three both over and outside of the SMA. Data assimilation mostly removed the positive SO₂ bias above approximately 800 hPa, because of the reduced surface emissions by OMI SO₂ measurements (c.f., Section 5). In the lower troposphere, however, data assimilation led to negative SO₂ biases. This probably reflects errors in local emissions, model processes within the boundary layer, vertical transport between the lower and middle troposphere, and in the assimilated retrievals and setting (e.g., constant retrieval errors were assumed for OMI SO₂). Further, the assimilated SO₂ column measurements will have a reduced sensitivity near the surface compared to the free troposphere, but this effect was not considered in the observation operator because of the lack of information in the retrievals. The model underestimated PAN below approximately 850 hPa over the SMA and throughout the troposphere outside of the SMA, whereas data assimilation reduced the negative bias associated with the increased NO₂.

The model overestimates the mean OH concentration by up to a factor of two in the lower troposphere and underestimates it by up to 35% in the upper troposphere. The overestimation in the lower troposphere is smaller (by approximately 25%) outside of the SMA. The data assimilation increases OH above approximately 700 hPa, showing a closer agreement with the observed profiles with bias reductions of 75–95% in the middle and upper troposphere (between 650–350 hPa), whereas the improvement is small in the lower troposphere. The increase in ozone increased OH throughout the free troposphere, while the increase in CO decreased OH in the lower troposphere. These adjustments led to a closer agreement with the observed OH profile outside of the SMA. As OH modulates the chemical lifetimes of many species and improves emission inversions (Miyazaki et al., 2012b, 2015, 2017), the significant improvements in OH confirm the usefulness of multiple-species assimilation in tropospheric chemistry analysis.

Model errors remain in the analysis of some non-assimilated species; these include overestimations in HNO₃, HO₂ and H₂O₂ in the lower and middle troposphere both over and outside of the SMA, and underestimations in CH₂O in the lower troposphere over the SMA.

HNO₃ is removed from the troposphere by deposition processes, while the chemical production of HNO₃ drives the observed increase in HNO₃ toward the surface over polluted areas. The large positive bias in the simulated HNO₃ could be caused by too weak depositions and/or too strong chemical productions. In addition, an underestimated formation of nitrate aerosol, due to the lack of formation with sea-salt particles and dust in the model, could be one of the causes of the overestimation of HNO₃ in the lower troposphere. Further investigations, for instance, using in-situ measurements of deposition and aerosol concentration would facilitate in improving the model performance.

The model includes the heterogeneous HO₂ loss by aerosols and cloud droplets. However, it assumes the final product of this HO₂ reaction to be H₂O₂ not H₂O. The absence of this loss process could lead to the overestimations in H₂O₂ and HO₂, as suggested by Mao et al. (2013). Kanaya et al. (2006) and (2016) discussed that inclusion of this loss would reduce daytime maxima of HO₂ and daytime net ozone production rate at Mt. Tai, in the center of the North China Plain and at Fukue Island, near Korea, respectively.

A lack of direct observational constraints limits improvements on these species. For instance, the assimilated satellite measurements contain limited information to reduce model errors due to fast chemistry such as model processes that determine the NO₂/NO ratio. The remaining model errors prevent the data assimilation improvement, e.g., in NO in the boundary layer, both over and outside of the SMA. Further, model errors in transient transport processes, e.g., owing to convection and boundary layer mixing, and in PBL mixing may yield errors in the NO profiles because the NO₂/NO ratio changes with height. The remaining errors after data assimilation are generally larger over the SMA than outside the SMA for several species (CO, SO₂, NO₂, NO, PAN, and OH). The spatial representativeness errors due to the limited resolution of the model could contribute to the disagreement over the SMA.

Any systematic error in the model processes will have a negative influence on the analysis including the emission estimates. For instance, the underestimation in SO₂ within the boundary layer could suggest a possible overestimation of an atmospheric sink of SO₂ in the model, which will result in an overestimation in estimated SO₂ emissions. From model sensitivity calculations, simulated SO₂ concentrations in the boundary layer were found to be sensitive to model parameters such as the heterogeneous reaction rate on dust surfaces. Changes in the chemical scheme are expected to affect the estimated sources. Similarly, an overestimate of NO_x removal processes could lead to an overestimation in NO_x emissions. Assimilating additional observations and adjusting more model parameters (e.g., VOC emissions, deposition, and/or chemical reactions rates) could be required to reduce model errors in these species and improve emissions estimates.

Figure 8 compares the spatial distribution of the tropospheric NO₂ column between the OMI measurements, model simulation, and data assimilation. The model overestimates high NO₂

columns over polluted areas in China and underestimates it over the Korean peninsula and the oceans. The area mean bias is -1.5×10^{15} molecules cm^{-2} (approximately 50% of the regional mean concentration) for South Korea and $+1.7 \times 10^{15}$ molecules cm^{-2} (approximately 75%) for eastern China. The a priori emissions were constructed for the year 2010. The simulation did not consider the influence of a rapid NO_x emission reduction after 2010 for China that was reported by Miyazaki et al. (2017) and Liu et al. (2017). For South Korea, most of the top-down estimates revealed increases after 2010 (Ding et al., 2017). The use of the 2010 emissions, along with large uncertainty in emission factors, could explain a part of the overestimation over China and the underestimation over South Korea. Data assimilation increases tropospheric NO₂ columns by approximately 1.4×10^{15} molecules cm^{-2} over South Korea and by $0.4\text{--}1.0 \times 10^{15}$ molecules cm^{-2} over the oceans and decreases over most of eastern China (by 3.5×10^{15} molecules cm^{-2} over northeastern China and by 5×10^{15} molecules cm^{-2} around Hangzhou and Shanghai). As expected, data assimilation greatly improved the agreements with the assimilated OMI measurements, with a reduced regional mean bias from 0.07 to 0.02×10^{15} molecules cm^{-2} and RMSE from 1.5 to 0.7×10^{15} molecules cm^{-2} , and an increased spatial correlation from 0.86 to 0.93 for the monthly mean fields for East Asia (defined as $30\text{--}45^\circ\text{N}$, $90\text{--}130^\circ\text{E}$). The model negative bias was reduced by approximately 40% (from 4 to 2.6×10^{15} molecules cm^{-2}) over Seoul and by 70% (from 1.4 to 0.4×10^{15} molecules cm^{-2}) for the country-average concentration in South Korea.

3.3 Impact of individual assimilated measurements

To demonstrate the relative importance of individual assimilated measurements on the improvements in the ozone profile analysis, we conducted Observing System Experiments (OSEs), by separately assimilating individual measurements into the data assimilation system. The total averaged changes in ozone by the multiple-constituent data assimilation over South Korea reached approximately 10 ppbv in the lower troposphere and approximately 20 ppbv in the middle and upper troposphere (c.f., Section 3.1.1).

As shown in Fig. 9, for the lower tropospheric ozone analysis, NO_x emission optimization by OMI and GOME-2 NO₂ data assimilation was most important. The NO₂ impact generally increased with decreasing latitude over the East Asia domain because of greater ozone production efficiency by NO_x and larger corrections made to regional NO_x emissions at lower latitudes; meanwhile, the impact around the South Korea varies largely with meteorological conditions. At 700 hPa, the smaller contribution in phase 1 around South Korea is associated with weak influences of either Korean and Chinese emissions, whereas the large contributions in phases 2–4 are associated with enhanced ozone productions through local (in phases 2 and 4) and remote (in phase 3) emissions.

The changes in NO_x emissions increased mean ozone concentration by 5.3 ± 0.6 ppbv (5.5 ± 0.7 ppbv) in phase 1 and by $6.0\text{--}6.3 \pm 0.3\text{--}0.7$ ppbv ($6.1\text{--}6.2 \pm 0.3\text{--}0.9$ ppbv) in phase 2–4 over the SMA (over South Korea) at 700 hPa. Below 800 hPa over the SMA (figure not shown),

the NO₂ assimilation explains most of the increase in mean ozone concentrations, except in the case of phase 4. The impact of NO_x emission optimization on the boundary layer ozone (at 900 hPa, figure not shown) reached 7.5 ± 1.6 ppbv in phase 4 over South Korea at 900 hPa (in contrast to 4.9–6.2 ppbv in other phases). By assimilating all the measurements, the total ozone increase reached 10.8 ± 3.8 ppbv in phase 2 and 10.7 ± 3.2 ppbv in phase 4 at 700 hPa (in contrast to 7.8–8.9 ppbv in other phases) and 12.0 ± 2.0 ppbv in phase 4 at 900 hPa (in contrast to 2.8–7.2 ppbv in other phases) over the SMA.

Fig. 10 compares the OSE results with the DC-8 aircraft measurements over SMA. The NO₂ assimilation leads to large error reductions both at 700 and 400 hPa, mostly throughout the campaign period. Assimilation of stratospheric MLS ozone measurements provides additional important corrections to the middle and upper tropospheric ozone, with up to 10 ppbv positive increments over South Korea and other areas in East Asia. Assimilation of MOPITT CO data mostly increased mean ozone concentration by 1–4 ppbv across the troposphere. The MLS impact in the middle and upper troposphere is large in phase 2, with mean bias reductions relative to the DC-8 measurements of 35% at 700 hPa and 38% at 400 hPa. In contrast, the total adjustment is largely dominated by the NO₂ assimilation throughout the troposphere in phase 3, reflecting the strong transport of polluted air from China, which reduces the mean bias by 45% at 700 hPa and 54 % at 400 hPa. The MLS impact reaches to lower tropospheric levels, particularly in phase 4.

These results demonstrate that the simultaneous optimization of concentration and emissions from multi-constituent data assimilation is an efficient method to correct the entire tropospheric ozone profile in East Asia and that the assimilation efficiency of individual measurements is dependent on the particular phase.

4 Assimilation of AIRS/OMI tropospheric ozone profiles

Here, we evaluate the impact of assimilating the AIRS/OMI multispectral tropospheric ozone profile analysis during the campaign. We conducted two additional data assimilation experiments: one assimilates only AIRS/OMI retrievals (AIRS/OMI DA), and the other assimilates the AIRS/OMI retrievals together with other assimilated retrievals used in the standard data assimilation calculation (Reanalysis+AIRS/OMI DA). Both the global (GL) and regional (RE for East Asia: 20–50°N, 80–130°E with denser spatial sampling) products were assimilated. The evaluation results at 510 hPa are depicted in Figure 11 and the statistics are summarized in Table 2. The model underestimated the monthly mean ozone concentrations by 4–28 ppbv in the tropics and overestimated by up to about 20 ppbv in the southern mid-latitudes relative to the AIRS/OMI retrievals at 510 hPa. Even without assimilating the AIRS/OMI retrievals, the reanalysis showed closer agreement with the AIRS/OMI retrievals than the model simulation for both the global and regional products, with a zonal mean bias of 3.9 ppbv in the extratropics of both hemispheric and -1.8 ppbv in the tropics for GL, and 0.9 ppbv for RE at 510

hPa. These results suggest good performance of both reanalysis and AIRS/OMI retrievals. By assimilating AIRS/OMI retrievals (AIRS/OMI DA), the ozone analysis shows closer agreement with AIRS/OMI retrievals than the model and reanalysis for most cases, confirming the capability of the AIRS/OMI data product for use in data assimilation. The zonal mean bias (RMSE) was reduced by 77% (36%) in the NH extratropics, 57% (50%) in the tropics, and 97% (55%) in the southern hemisphere for GL, and 98% (43%) for RE at 510 hPa, compared with the model simulation results. Improvements can be found throughout the troposphere, with reduced improvements in the lower troposphere (i.e., at 750 hPa).

As shown in Figure 12 (upper panels), the mean analysis spread is larger by up to 70% in all phases in AIRS/OMI DA than in the standard data assimilation calculation without any ozone assimilation (c.f., Fig. 6). The analysis spread is expected to decrease when effective observations are assimilated. In AIRS/OMI DA, the spread was mainly increased by the covariance inflation process in ozone data assimilation (c.f., Section 2.2.2). The analysis spread in the AIRS/OMI data assimilation (typically 6–8 ppbv over South Korea) provides better agreements with the actual analysis and observation difference (i.e., 6.1 ± 4.5 ppb for the lower troposphere) than that in the standard data assimilation calculation (3.9 ± 1.2 ppb), which can be regarded as a more realistic estimate of analysis uncertainty. Note that the applied covariance inflation factor was chosen to obtain the best agreement with the observed ozone profiles.

The AIRS/OMI observation coverage and retrieval uncertainty were similar between different phases (except after 29 May when OMI went into survival model and ceased operation). However, the ozone analysis increments from AIRS/OMI assimilation varied substantially with meteorological conditions (lower panels in Fig. 12). The analysis increment was large over central and southern China in phase 1 and around the Korean peninsula in phase 3. In phase 2, the small increment over East Asia corresponds to the small background spread. These results suggest that the data assimilation efficiency of both direct ozone measurements and precursor measurements (c.f., Section 3.1.4) varied greatly with meteorological conditions, associated with changes in the background error covariance.

The varying data assimilation efficiency can also be confirmed from evaluations using the DC-8 measurements. As shown by Fig 13, assimilation of AIRS/OMI data alone (AIRS/OMI DA) reduced the mean model bias with respect to the mean DC-8 ozone profiles in the middle troposphere by approximately 90% in phases 1 and 2 and by approximately 70% in phase 4. The bias reduction was smaller in phase 3 (by 35%), which is thought to be associated with the smaller spread and analysis increments in phase 2. With adding AIRS/OMI assimilation in the standard data assimilation calculation (Reanalysis+AIRS/OMI DA), the error reduction reaches larger than 80% in all phases, while providing improved error estimates similar to those in AIRS/OMI DA. As an exception, the error reduction became slightly smaller by adding AIRS/OMI assimilation in phase 3. The current AIRS/OMI data is only using a small fraction of the available observations. The impact of AIRS/OMI could become significantly greater when

more data is processed. These results suggest that combining precursors' emission optimization and direct ozone assimilation is an effective method to improve the tropospheric ozone profile analysis, independent from meteorological conditions.

5 Estimated emission sources

Figure 14 shows regional maps of surface emissions of NO_x, CO, and SO₂ estimated from data assimilation and the difference from a priori emissions (constructed based on HTAP-version 2 inventories) averaged during May 2016. Data assimilation increases NO_x emissions over some parts of urban East Asia, such as over Beijing (by 10%), around Shanghai (by 10%–50%), Hong Kong (14%), Shenzhen (20%), Seoul (22%), and Busan (54%). The positive increments suggest underestimations in anthropogenic emissions in the inventories. In contrast, the increments are negative over central China (by 10%–50%). The complex spatial structure in the increments indicates large uncertainties in the emission inventories and different emission biases among cities. The use of the 2010 a priori emissions could also explain the spatial structure of the analysis increment. Over central China, large negative increments can be associated with recent emission reductions since 2011, as revealed by Miyazaki et al. (2017), Liu et al. (2017), and Qu et al. (2017). The large adjustments over South Korea could also be associated with large uncertainties in emission factor and activity used in the inventories (Kim et al., 2013).

The CO emissions increased over most of China, with large increases in northwestern and southeastern China by 10%–40%. The overall increases can be attributed to emission underestimations in inventories and high bias in northern hemispheric OH, as discussed by Strode et al. (2016). Conversely, the decrease in CO emissions over central-eastern China could be associated with the reported decrease in emissions after 2010 (Jiang et al., 2017). The spatial pattern in NO_x and CO emissions largely differed,

The SO₂ emissions decreased by 10%–90% over the entire East Asia domain, with large reductions observed over central and southwestern China. These variations are considered to be associated with the reductions in China's total regional emissions after 2010, as reported by Koukouli et al. (2018), and large uncertainties in the inventories. The extent of reductions in SO₂ emissions was smaller over northwestern China. This could be associated with the exceptional positive trend in this region after 2010 (Ling et al., 2017).

Table 3 summarizes the total regional emissions of NO_x, CO, and SO₂ for South Korea (125–129.5°E, 34.2–38.2°N) and eastern China (100–124°E, 21–43°N) obtained from several bottom-up inventories and estimated through top-down estimates approaches by using two different NO₂ retrieval products from the QA4ECV version 1.1 (Boersma et al., 2017a, 2017b) and DOMINO version 2 (Boersma et al., 2004, 2011) for OMI and GOME-2 but the same observations of other trace gases. Bottom-up emissions were obtained from the HTAP version 2

for 2010 (Janssens-Maenhout et al., 2015), EDGAR version 4.3.2 for 2012 (Crippa et al., 2018), and KORUS-AQ version 2 inventories. The KORUS-AQ version 2 emissions were constructed based on the improved CAPSS (Clean Air Policy Support System) 2015 emissions for South Korea (Lee et al., 2011), and the Comprehensive Regional Emissions for Atmospheric Transport Experiment (CREATE) version 3 for China for 2015 using the SMOKE-Asia emission processing at 0.1° resolution (Woo et al., 2012). A top-down NO_x estimation for 2016, based on the DECSO v5.1qa inversion using the OMI QA4ECV v1.1 NO₂ products (Ding et al., 2018), and the v1 emission estimates for SO₂ using the OMI SO₂ BIRA products (Koukouli et al., 2018) for 2014 at 0.25° resolution were obtained through the GlobEmission project (van der A et al., 2017).

There are large differences between the NO_x emission inventories for South Korea (0.30–0.43 TgN) and eastern China (6.2–8.3 TgN), as similarly discussed by Ding et al. (2017) for 2005–2015. In South Korea, the top-down emissions of NO_x emissions estimated using QA4ECV is 0.42 TgN, which is about 40% higher than the KORUS v2 and HTAP v2 inventories, but is equivalent to the EDGAR v4.3.2 inventories. Compared with the GlobEmission top-down estimate, the estimated NO_x emissions were higher by 13%, which could be attributed to the coarser model resolution dilution effects and non-linear chemistry as well as differences in model chemistry. The top-down emission of NO_x in eastern China is similar to the HTAP v2 emissions, while the spatial distribution is largely different (c.f., Fig. 14).

When the DOMINO product is used instead of the QA4ECV product, the estimated NO_x emissions for South Korea and eastern China are about 5% and 3%, respectively, lower. This reflects the updated retrievals including revised a priori profiles and improved uncertainty estimates. Although higher emissions are estimated by the QA4ECV product, the retrieved tropospheric columns are generally smaller for polluted areas, associated with the lower a priori column in the QA4ECV product and the use of the averaging kernel (Eskes and Boersma, 2003). Changes made to retrieval errors in the retrieval products could also be important for obtaining sufficient emission corrections when using the QA4ECV product, especially for highly polluted areas. Because of the improved error estimates in the QA4ECV product, we used the original retrieval error for both products in this study, unlike in our previous study (Miyazaki et al., 2017), which reduced retrieval errors of individual NO₂ retrievals by 30 % over polluted areas for the DOMINO product.

The top-down CO emission for South Korea is 1.1 TgCO, which is 22% higher than the KORUS v2 emissions and 83% higher than the HTAP v2 emission. However, it is approximately 40% of the EDGAR v4.3.2 emissions. The total CO emission in eastern China varies from 107.5 TgCO (EDGAR v4.3.2) to 231.3 TgCO (HTAP v2) among the inventories; the top-down emission is approximately 19% higher (231.3 TgCO) than the a priori emissions (i.e., HTAP v2). The EDGAR v4.2 emission is more than 50% lower than the top-down estimate for eastern China.

The a posteriori estimates for total SO₂ emissions in South Korea are approximately 40% lower than the HTAP v2 emissions and 73% lower than the KORUS-AQ v2 emissions. In eastern China, the a posterior estimates are 65% lower than the HTAP v2 emissions and 85% lower than the EGDAR v4.3.2 emissions. These results suggest large overestimations of SO₂ emissions in the bottom-up emission inventories. The overestimations could also be partly due to the recent rapid emission reduction (Li et al., 2017). However, since the a posteriori emission led to underestimations in the boundary layer SO₂ concentrations with respect to the DC-8 measurements (c.f., Fig. 7), the estimated emission in South Korea could be underestimated, associated with the large uncertainty (e.g., random noise of ~0.5 DU for remote areas, as described in Li et al (2013)) and the assumed constant retrieval errors and air mass factor because of lack of information in the assimilated OMI SO₂ retrievals.

The estimated NO_x emissions were sensitive to forecast model resolution. The estimated NO_x emissions became approximately 10% larger in coarser resolution (2.8°×2.8°) analyses than in fine resolution (1.1°×1.1°) analyses for South Korea, using the same data assimilation setting. Sekiya et al. (2017) demonstrated that coarser resolution models tend to underestimate the tropospheric NO₂ column over polluted areas associated with dilution effects and non-linear chemistry. Further increases in model resolution could be crucial to obtain reasonable estimates for the highly polluted cases that are pronounced in East Asia, as discussed by Valin et al. (2011) and Sekiya et al. (2017).

Using the optimized emission data sets, we conducted model sensitivity calculations to estimate the impact of precursors' emissions from different regions on the ozone amount over Seoul. This will be presented in a separate companion study.

6 Conclusions

Comprehensive chemical reanalyses of multi-constituent concentration and emissions fields, provided by an assimilation of multiple satellite measurements of ozone, CO, NO₂, HNO₃, PAN, and SO₂ from OMI, GOME-2, MOPITT, MLS, and AIRS, are used to understand the processes controlling variations in air pollution over East Asia during the KORUS-AQ campaign of May–June 2016. Various measurements obtained during the KORUS-AQ provide an opportunity to evaluate data assimilation performance and the value of existing satellite platforms to study air quality over East Asia.

The evaluation of the data assimilation fields demonstrates the importance of multiple species satellite data assimilation and the simultaneous optimization of the concentration and emission fields. The analyzed ozone, CO, NO₂, SO₂, and OH profiles showed improved agreements with DC-8 aircraft measurements from the lower troposphere to the lower stratosphere. Corrections made to the precursors emissions (i.e., NO_x and CO emissions) were important in reducing the lower and middle tropospheric model ozone bias, while direct

concentration adjustment by ozone measurements in the UTLS played important roles in correcting the middle and upper tropospheric ozone. The negative bias in OH was also largely reduced in the free troposphere because of the combined assimilation of multiple species, which played an important role in propagating observational information among various species and in modifying the chemical lifetimes of various reactive gases. We also tested the assimilation of AIRS/OMI multispectral retrievals of tropospheric ozone profiles. An additional bias reduction on the tropospheric ozone analysis, especially in the middle troposphere, was obtained by assimilating the multispectral retrievals, which was also important to obtain realistic estimates of the analysis uncertainty.

Both the model performance and data assimilation efficiency were sensitive to meteorological conditions. The observed boundary layer ozone concentration over Seoul exceeded 90 ppbv for stagnant condition, but was 10–30 ppbv lower for dynamic weather conditions. Large reductions on the free tropospheric model bias by data assimilation were found throughout the campaign. In contrast, the lower tropospheric ozone bias was only slightly reduced for stagnant and transboundary transport conditions. During these phases, errors in local photochemical processes and precursor emissions could prevent improvements in the lower tropospheric ozone. In contrast, for dynamic weather conditions, observational information was propagated efficiently in time and space, improving the data assimilation performance throughout the troposphere. Assimilation of AIRS/OMI retrievals provided the largest corrections for dynamic weather conditions, whereas the improvement was limited just after stagnant conditions because of small background spread in the previous time period. However, expected increases in AIRS/OMI data density could further ameliorate the performance. Our analysis suggests that combining precursors' emission optimization and direct ozone assimilation is an effective method to obtain sufficient corrections on ozone for any meteorological condition. To remove the influence of persistent model error and to further improve ozone analysis, adjusting additional model parameters, such as VOC emissions, deposition, and/or chemical reaction rates, and optimizing model error covariance could also be important.

Estimated NO_x emissions were 0.42 TgN in South Korea, which were 40% higher as compared with the KORUS v2 and HTAP v2 inventories. The data assimilation result suggests an important underestimation of anthropogenic sources in emission inventories. Total CO emissions for South Korea from data assimilation are higher than the KORUS v2 by 22% and the HTAP v2 by 83 %, but it is 40% of the EGDAR v4.3.2 emissions. The updated emissions of NO_x and CO increased mean ozone concentration by approximately 6 ppbv at 700 hPa over the SMA and South Korea and by up to 7.5±1.6 ppbv over South Korea within the boundary layer when a blocking pattern determined the large-scale ozone distribution. For SO₂, estimated emissions are 40%–73% lower than the KORUS v2 and HTAP v2 inventories for South Korea and approximately 65% lower than the HTAP v2 emissions in eastern China. The optimized emissions can be expected to provide an accurate estimate of the source-receptor relationship,

such as the impact of precursors' emissions from different regions on the ozone amount over Seoul. This will be presented in a separate companion paper (Miyazaki et al., *to be submitted*).

Data assimilation analysis provides comprehensive information on the spatial and temporal variations of global ozone; in this study, it was also used to measure the representativeness of the DC-8 aircraft observations. Our investigation using reanalysis shows that the mean ozone concentration averaged during the campaign was persistently higher over the SMA (75.1 ± 7.6 ppbv) than over the broader KORUS-AQ domain (70.5 ± 9.2 ppbv), with the largest mean concentration (79.8 ± 4.1 ppbv) over the SMA for stagnant conditions at 700 hPa. Our analysis also demonstrated that the DC-8 measurements provide concentrations that may be considered representative of the monthly mean over the SMA, but largely overestimate area mean concentrations of the KORUS-AQ domain by up to 6 ppbv in the lower troposphere.

Although the assimilation of multi-constituent data provides comprehensive constraints on the entire chemical system and reduces the uncertainty on the emission estimates, the influences of model and observation errors remain a concern. Model performance is critical for the correct propagation of observational information between chemical species and to improve the emission estimation. Biases in the assimilated measurements may seriously degrade the data assimilation analysis including the emission estimation, as discussed in our previous studies (Miyazaki et al., 2012a; 2015; Miyazaki and Eskes, 2013). Application of a bias correction procedure for multiple measurements could improve the data assimilation performance. The relatively coarse model resolution ($1.1^\circ \times 1.1^\circ$) is insufficient to resolve local air pollution, which will limit improvements in the data assimilation in urban areas close to the surface.

Chemical reanalysis data based on the EnKF approach also has the potential to provide information on long-term and regional variations of background ozone levels (Miyazaki et al., 2015). Such detailed information on regional scale ozone variations cannot be obtained from any individual measurements. Our results also confirmed the great potential of advanced tropospheric ozone retrievals to improve tropospheric ozone profile analysis in combination with precursor emission optimization. In the future, assimilating datasets from a new constellation of LEO sounders (e.g., IASI, AIRS, CrIS, Sentinel-5P [TROPOMI], and Sentinel-5) and GEO satellites such as GEMS will provide more detailed knowledge of ozone and its precursors for East Asia (Bowman, 2013).

Acknowledgments

We acknowledge the use of data products from the NASA AURA, EOS Terra, and Aqua satellite missions. Support from the NASA ROSES-2013 Atmospheric Composition: Aura Science Team program (grant number: NNN13D455T) on MUSES algorithm development for joint AIRS+OMI ozone retrievals is gratefully acknowledged. Part of the research was carried out at the Jet Propulsion Laboratory, California Institute of Technology, under a contract with the National Aeronautics and Space Administration. We also acknowledge the free use of

tropospheric NO₂ column data from the SCIAMACHY, GOME-2, and OMI sensors from <http://www.qa4ecv.eu> and www.temis.nl. We thank the KORUS-AQ team (R.C. Cohen, M. Yang, P. Wennberg, A. Fried, G.S. Diskin, W. Brune, and A. Weinheimer) for the aircraft observational data. We would also like to thank the editor and three anonymous reviewers for their valuable comments. This work was supported through JSPS KAKENHI grant numbers 15K05296, 26220101, 26287117, and 18H01285, the Coordination Funds for Promoting AeroSpace Utilization by MEXT, JAPAN, and by the Post-K computer project Priority Issue 4 - Advancement of meteorological and global environmental predictions utilizing observational Big Data. The Earth Simulator was used for simulations as "Strategic Project with Special Support" of Japan Agency Marine-Earth Science and Technology. The National Center for Atmospheric Research is funded by the National Science Foundation. B. Gaubert, J. Barre, L. Emmons acknowledge support from the NASA KORUS-AQ grant NNX16AD96G.

Data

The chemical reanalysis data can be downloaded through our web site (<https://ebcrpa.jamstec.go.jp/~miyazaki/tcr/>)

References

- Akimoto, H. (2003), Global air quality and pollution. *Science*, 302, 1716-1719. doi:10.1126/science.1092666.
- Andres, R. J., & A. D. Kasgnoc (1998), A time-averaged inventory of subaerial volcanic sulfur emissions, *J. Geophys. Res.*, 103(D19), 25,251–25,261, doi:10.1029/98JD02091.
- Bocquet, M., Elbern, H., Eskes, H., Hirtl, M., Žabkar, R., Carmichael, G. R., Flemming, J., Inness, A., Pagowski, M., Pérez Camaño, J. L., Saide, P. E., San Jose, R., Sofiev, M., Vira, J., Baklanov, A., Carnevale, C., Grell, G., & Seigneur, C. (2015), Data assimilation in atmospheric chemistry models: current status and future prospects for coupled chemistry meteorology models, *Atmos. Chem. Phys.*, 15, 5325–5358, <https://doi.org/10.5194/acp-15-5325-2015>.
- Boersma, K. F., Eskes, H. J., & Brinksma, E. J. (2004), Error Analysis for Tropospheric NO₂ Retrieval from Space, *J. Geophys. Res.*, 109, D04311, <https://doi.org/10.1029/2003JD003962>.
- Boersma, K. F., Eskes, H. J., Dirksen, R. J., van der A, R. J., Veefkind, J. P., Stammes, P., Huijnen, V., Kleipool, Q. L., Sneep, M., Claas, J., Leitão, J., Richter, A., Zhou, Y., & Brunner, D. (2011), An improved tropospheric NO₂ column retrieval algorithm for the Ozone Monitoring Instrument, *Atmos. Meas. Tech.*, 4, 1905–1928, <https://doi.org/10.5194/amt-4-1905-2011>.
- Boersma, K. F., Eskes, H., Richter, A., De Smedt, I., Lorente, A., Beirle, S., Van Geffen, J., Peters, E., Van Roozendael, M. & Wagner, T., (2017a). QA4ECV NO₂ tropospheric and stratospheric vertical column data from OMI (Version 1.1) [Data set]. Royal Netherlands Meteorological Institute (KNMI). <http://doi.org/10.21944/qa4ecv-no2-omi-v1.1>

949 Boersma, K. F., Eskes, H., Richter, A., De Smedt, I., Lorente, A., Beirle, S., Van Geffen, J.,
 950 Peters, E., Van Roozendael, M. & Wagner, T., (2017b). QA4ECV NO₂ tropospheric and
 951 stratospheric vertical column data from GOME-2A (Version 1.1) [Data set]. Royal Netherlands
 952 Meteorological Institute (KNMI). <http://doi.org/10.21944/qa4ecv-no2-gome2a-v1.1>

953 [Boersma, K. F., Eskes, H. J., Richter, A., De Smedt, I., Lorente, A., Beirle, S., van Geffen, J. H.](#)
 954 [G. M., Zara, M., Peters, E., Van Roozendael, M., Wagner, T., Maasakkers, J. D., van der A, R.](#)
 955 [J., Nightingale, J., De Rudder, A., Irie, H., Pinardi, G., Lambert, J.-C., and Compernelle, S.:](#)
 956 [Improving algorithms and uncertainty estimates for satellite NO₂ retrievals: Results from the](#)
 957 [Quality Assurance for Essential Climate Variables \(QA4ECV\) project, Atmos. Meas. Tech.](#)
 958 [Discuss., <https://doi.org/10.5194/amt-2018-200>, in review, 2018.](#)

959 Boersma, K. F., J. van Geffen, H. Eskes, R. van der A, I. De Smedt, M. Van Roozendael, H. Yu,
 960 A. Richter, E. Peters, S. Beirle, T. Wagner, A. Lorente, T. Scanlon, S. Compernelle, J.-C.
 961 Lambert (2017c), Product Specification Document for the QA4ECV NO₂ ECV precursor
 962 product, Royal Netherlands Meteorological Institute (KNMI), available at
 963 http://temis.nl/qa4ecv/no2col/QA4ECV_NO2_PSD_v1.1.compressed.pdf

964 Bovensmann, H., Burrows, J. P., Buchwitz, M., Frerick, J., Noël, S., Rozanov, V. V., Chance, K.
 965 V., & Goede, A. P. H. (1999), SCIAMACHY: mission objectives and measurement modes, *J.*
 966 *Atmos. Sci.*, 56, 127–150.

967 Bowman, K. W., Shindell, D. T., Worden, H. M., Lamarque, J. F., Young, P. J., Stevenson, D.
 968 S., Qu, Z., de la Torre, M., Bergmann, D., Cameron-Smith, P. J., Collins, W. J., Doherty, R.,
 969 Dalsøren, S. B., Faluvegi, G., Folberth, G., Horowitz, L. W., Josse, B. M., Lee, Y. H.,
 970 MacKenzie, I. A., Myhre, G., Nagashima, T., Naik, V., Plummer, D. A., Rumbold, S. T., Skeie,
 971 R. B., Strode, S. A., Sudo, K., Szopa, S., Voulgarakis, A., Zeng, G., Kulawik, S. S., Aghedo, A.
 972 M., and Worden, J. R. (2013), Evaluation of ACCMIP outgoing longwave radiation from
 973 tropospheric ozone using TES satellite observations, *Atmos. Chem. Phys.*, 13, 4057–4072,
 974 <https://doi.org/10.5194/acp-13-4057-2013>.

975 Bowman, K. W. (2013), Toward the next generation of air quality monitoring: Ozone, *Atmos.*
 976 *Environ.*, 80, 571–583, <https://doi.org/10.1016/j.atmosenv.2013.07.007>.

977 Brune, W. H., Stevens, P. S., & Mather, J. H. (1995), Measuring OH and HO₂ in the
 978 Troposphere by Laser Induced Fluorescence at Low Pressure, *J. Atmos. Sciences* 52, 3328–3336.

979 Callies, J., Corpaccioli, E., Eisinger, M., Hahne, A., and Lefebvre, A. (2000), GOME-2 –
 980 MetOp’s second generation sensor for operational ozone monitoring, *ESA Bull.-Eur. Space*, 102,
 981 28–36.

982 Castellanos, P., Boersma, K. F., & van der Werf, G. R. (2014), Satellite observations indicate
 983 substantial spatiotemporal variability in biomass burning NO_x emission factors for South
 984 America, *Atmos. Chem. Phys.*, 14, 3929–3943, <https://doi.org/10.5194/acp-14-3929-2014>.

985 Clerbaux, C., Boynard, A., Clarisse, L., George, M., Hadji-Lazaro, J., Herbin, H., Hurtmans, D.,
 986 Pommier, M., Razavi, A., Turquety, S., Wespes, C., & Coheur, P.-F. (2009), Monitoring of
 987 atmospheric composition using the thermal infrared IASI/MetOp sounder, *Atmos. Chem. Phys.*,
 988 9, 6041–6054, <https://doi.org/10.5194/acp-9-6041-2009>.

989 Crippa, M., Guizzardi, D., Muntean, M., Schaaf, E., Dentener, F., van Aardenne, J. A., Monni,
 990 S., Doering, U., Olivier, J. G. J., Pagliari, V., and Janssens-Maenhout, G.: Gridded Emissions of
 991 Air Pollutants for the period 1970–2012 within EDGAR v4.3.2, *Earth Syst. Sci. Data Discuss.*,
 992 <https://doi.org/10.5194/essd-2018-31>, in review, 2018.

993 Crounse, J. D., McKinney, K. A., Kwan, A. J., & Wennberg, P. O. (2006), Measurement of gas-
 994 phase hydroperoxides by chemical ionization mass spectrometry, *Anal. Chem.*, 78, 6726–6732,
 995 doi:10.1021/ac0604235.

996 Dee, D. P., Uppala, S. M., Simmons, A. J., Berrisford, P., Poli, P., Kobayashi, S., Andrae, U.,
 997 Balmaseda, M. A., Balsamo, G., Bauer, P., Bechtold, P., Beljaars, A. C. M., van de Berg, L.,
 998 Bidlot, J., Bormann, N., Delsol, C., Dragani, R., Fuentes, M., Geer, A. J., Haimberger, L., Healy,
 999 S. B., Hersbach, H., Hólm, E. V., Isaksen, L., Kållberg, P., Köhler, M., Matricardi, M., McNally,
 1000 A. P., Monge-Sanz, B. M., Morcrette, J.-J., Park, B.-K., Peubey, C., de Rosnay, P., Tavolato, C.,
 1001 Thépaut, J.-N. and Vitart, F. (2011), The ERA-Interim reanalysis: configuration and performance
 1002 of the data assimilation system. *Q.J.R. Meteorol. Soc.*, 137: 553–597. doi:10.1002/qj.828

1003 Deeter, M. N., Edwards, D. P., Francis, G. L., Gille, J. C., Martinez-Alonso, S., Worden, H. M.,
 1004 & Sweeney, C. (2017), A Climate-scale Satellite Record for Carbon Monoxide: The MOPITT
 1005 Version 7 Product, *Atmos. Meas. Tech.*, 10, 2533–2555, [https://doi.org/10.5194/amt-10-2533-](https://doi.org/10.5194/amt-10-2533-2017)
 1006 [2017](https://doi.org/10.5194/amt-10-2533-2017).

1007 Ding, J., Miyazaki, K., van der A, R. J., Mijling, B., Kurokawa, J.-I., Cho, S., Janssens-
 1008 Maenhout, G., Zhang, Q., Liu, F., & Levelt, P. F. (2017), Intercomparison of NO_x emission
 1009 inventories over East Asia, *Atmos. Chem. Phys.*, 17, 10125–10141, [https://doi.org/10.5194/acp-](https://doi.org/10.5194/acp-17-10125-2017)
 1010 [17-10125-2017](https://doi.org/10.5194/acp-17-10125-2017).

1011 Ding, J., van der A, R. J., Mijling, B., Jalkanen, J.-P., Johansson, L. and Levelt, P. F., Maritime
 1012 NO_x emissions over Chinese seas derived from satellite observations. *Geophysical Research*
 1013 *Letters*, 45. <https://doi.org/10.1002/2017GL076788>, 2018.

1014 Eskes, H. J. & Boersma, K. F. (2003), Averaging kernels for DOAS total-column satellite
 1015 retrievals, *Atmos. Chem. Phys.*, 3, 1285–1291, <https://doi.org/10.5194/acp-3-1285-2003>.

1016 Flemming, J., Inness, A., Jones, L., Eskes, H. J., Huijnen, V., Schultz, M. G., Stein, O., Cariolle,
 1017 D., Kinnison, D., & Brasseur, G. (2011), Forecasts and assimilation experiments of the Antarctic
 1018 ozone hole 2008, *Atmos. Chem. Phys.*, 11, 1961–1977, [https://doi.org/10.5194/acp-11-1961-](https://doi.org/10.5194/acp-11-1961-2011)
 1019 [2011](https://doi.org/10.5194/acp-11-1961-2011).

1020 Flemming, J., Benedetti, A., Inness, A., Engelen, R. J., Jones, L., Huijnen, V., Remy, S.,
 1021 Parrington, M., Suttie, M., Bozzo, A., Peuch, V.-H., Akritidis, D., & Katragkou, E. (2017), The

1022 CAMS interim Reanalysis of Carbon Monoxide, Ozone and Aerosol for 2003–2015, *Atmos.*
 1023 *Chem. Phys.*, 17, 1945–1983, <https://doi.org/10.5194/acp-17-1945-2017>.

1024 Fioletov, V. E., McLinden, C. A., Krotkov, N., Li, C., Joiner, J., Theys, N., Carn, S., & Moran,
 1025 M. D. (2016), A global catalogue of large SO₂ sources and emissions derived from the Ozone
 1026 Monitoring Instrument, *Atmos. Chem. Phys.*, 16, 11497–11519, doi:10.5194/acp-16-11497-2016.

1027 Fioletov, V., McLinden, C. A., Kharol, S. K., Krotkov, N. A., Li, C., Joiner, J., Moran, M. D.,
 1028 Vet, R., Visschedijk, A. J. H., & Denier van der Gon, H. A. C. (2017), Multi-source SO₂
 1029 emission retrievals and consistency of satellite and surface measurements with reported
 1030 emissions, *Atmos. Chem. Phys.*, 17, 12597–12616, <https://doi.org/10.5194/acp-17-12597-2017>.

1031 Fu D., Worden J.R., Liu X., Kulawik S.S., Bowman K.W., & Natraj V. (2013), Characterization
 1032 of ozone profiles derived from Aura TES and OMI radiances, *Atmos. Chem. Phys.*, 13(6), 3,445–
 1033 3,462.

1034 Fu D., Kulawik S.S., Miyazaki K., Bowman K.W., Worden J.R., Eldering A., Livesey N.J.,
 1035 Teixeira J., Irion F.W., Herman R.L., Osterman G.B., Liu X., Levelt P., Thompson A.M., Strow
 1036 L.L., Luo M., (2018), Retrievals of tropospheric ozone profiles from the synergism of AIRS and
 1037 OMI: methodology and validation, *Atmos. Meas. Tech.*, in press.

1038 Fu D., Bowman K.W., Worden H., Natraj V., Yu S., Worden J.R., Veefkind P., Aben I.,
 1039 Landgraf J., Strow L., Han Y. (2016), High resolution tropospheric carbon monoxide profiles
 1040 retrieved from CrIS and TROPOMI, *Atmos. Meas. Tech.*, 9, 2567–579.

1041 Gaubert, B., Arellano Jr., A. F., Barré, J., Worden, H. M., Emmons, L. K., Tilmes, S., Buchholz,
 1042 R. R., Vitt, F., Raeder, K., Collins, N., Anderson, J. L., Wiedinmyer, C., Martinez Alonso, S.,
 1043 Edwards, D. P., Andreae, M. O., Hannigan, J. W., Petri, C., Strong, K., & Jones, N. (2016),
 1044 Toward a chemical reanalysis in a coupled chemistry-climate model: An evaluation of MOPITT
 1045 CO assimilation and its impact on tropospheric composition, *J. Geophys. Res.-Atmos.*, 121,
 1046 7310–7343, <https://doi.org/10.1002/2016JD024863>.

1047 George, M., Clerbaux, C., Hurtmans, D., Turquety, S., Coheur, P.-F., Pommier, M., Hadji-
 1048 Lazaro, J., Edwards, D. P., Worden, H., Luo, M., Rinsland, C., & McMillan, W. (2009), Carbon
 1049 monoxide distributions from the IASI/METOP mission: evaluation with other space-borne
 1050 remote sensors, *Atmos. Chem. Phys.*, 9, 8317–8330, <https://doi.org/10.5194/acp-9-8317-2009>.

1051 Graedel, T. E., Bates, T. S., Bouwman, A. F., Cunnold, D., Dignon, J., Fung, I., Jacob, D. J.,
 1052 Lamb, B. K., Logan, J. A., Marland, G., Middleton, P., Pacyna, J. M., Placet, M., & Veldt, C.
 1053 (1993), A compilation of inventories of emissions to the atmosphere, *Global Biogeochem. Cy.*, 7,
 1054 1–26.

1055 Henze, D. K., A. Hakami, & J. H. Seinfeld (2007), Development of the adjoint of GEOS-Chem,
 1056 *Atmos. Chem. Phys.*, 7, 2413–2433.

1057 Herman, R. L. and Kulawik, S. S. (Eds.) (2013), Tropospheric Emission Spectrometer TES
 1058 Level 2 (L2) Data User's Guide, D-38042, version 5.0, Jet Propulsion Laboratory, California
 1059 Institute of Technology, Pasadena, CA, available at: <http://tes.jpl.nasa.gov/documents> (last
 1060 access: 30 March 2018).

1061 Herman, R.(editor), D. Fu, S. Kulawik, K. Miyazaki, G. Osterman, K. Bowman, J. Worden, &
 1062 TES team (2017), AIRS/OMI Validation Report, Version 1.0, Jet Propulsion Laboratory,
 1063 California Institute of Technology, December 8, 2017.

1064 Houtekamer, P. L. & Mitchell, H. L. (2005), Ensemble Kalman filtering. *Q. J. R. Meteorol. Soc.*,
 1065 131: 3269–3289. doi:10.1256/qj.05.135

1066 Houtekamer PL, & Zhang F. (2016), Review of the ensemble Kalman filter for atmospheric data
 1067 assimilation. *Mon. Weather Rev.*, 144: 4489–4532.

1068 Huey, L. G. (2007), Measurement of trace atmospheric species by chemical ionization mass
 1069 spectrometry: Speciation of reactive nitrogen and future directions, *Mass Spectrom. Rev.*, 26(2),
 1070 166-184.

1071 Hunt, B. R., Kostelich, E. J., & Szunyogh, I. (2007), Efficient data assimilation for
 1072 spatiotemporal chaos: a local ensemble transform Kalman filter, *Physica D*, 230, 112–126.

1073 Inness, A., Baier, F., Benedetti, A., Bouarar, I., Chabrillat, S., Clark, H., Clerbaux, C., Coheur,
 1074 P., Engelen, R. J., Errera, Q., Flemming, J., George, M., Granier, C., Hadji-Lazaro, J., Huijnen,
 1075 V., Hurtmans, D., Jones, L., Kaiser, J. W., Kapsomenakis, J., Lefever, K., Leitão, J., Razinger,
 1076 M., Richter, A., Schultz, M. G., Simmons, A. J., Suttie, M., Stein, O., Thépaut, J.-N., Thouret,
 1077 V., Vrekoussis, M., Zerefos, C., & the MACC team (2013), The MACC reanalysis: an 8yr data
 1078 set of atmospheric composition, *Atmos. Chem. Phys.*, 13, 4073–4109,
 1079 <https://doi.org/10.5194/acp-13-4073-2013>.

1080 Janssens-Maenhout, G., Crippa, M., Guizzardi, D., Dentener, F., Muntean, M., Pouliot, G.,
 1081 Keating, T., Zhang, Q., Kurokawa, J., Wankmüller, R., Denier van der Gon, H., Kuenen, J. J.
 1082 P., Klimont, Z., Frost, G., Darras, S., Koffi, B., & Li, M. (2015), HTAP v2.2: a mosaic of
 1083 regional and global emission grid maps for 2008 and 2010 to study hemispheric transport of air
 1084 pollution, *Atmos. Chem. Phys.*, 15, 11411–11432, doi:10.5194/acp-15-11411-2015.

1085 Jiang, Z., Worden, J. R., Worden, H., Deeter, M., Jones, D. B. A., Arellano, A. F., & Henze, D.
 1086 K. (2017), A 15-year record of CO emissions constrained by MOPITT CO observations, *Atmos.*
 1087 *Chem. Phys.*, 17, 4565-4583, <https://doi.org/10.5194/acp-17-4565-2017>.

1088 Jiang, Z., B. C. McDonald, H. Worden, J. R. Worden, K. Miyazaki, Z. Qu, D. K. Henze, D. B. A.
 1089 Jones, A. F. Arellano, E. V. Fischer, L. Zhu, and K. F. Boersma (2018), Unexpected slowdown
 1090 of US pollutant emission reduction in the last decade, *Proceedings of the National Academy of*
 1091 *Sciences*, 201801191; DOI: 10.1073/pnas.1801191115.

1092 Jones, D. B. A., Bowman, K. W., Palmer, P. I., Worden, J. R., Jacob, D. J., Hoffman, R. N., Bey,
 1093 I., & Yantosca, R. M. (2013), Potential of observations from the Tropospheric Emission
 1094 Spectrometer to constrain continental sources of carbon monoxide, *J. Geophys. Res.-Atmos.*, 108,
 1095 4789, <https://doi.org/10.1029/2003JD003702>.

1096 Kanaya, Y., Pochanart, P., Liu, Y., Li, J., Tanimoto, H., Kato, S., Suthawaree, J., Inomata, S.,
 1097 Taketani, F., Okuzawa, K., Kawamura, K., Akimoto, H., and Wang, Z. F.: Rates and regimes of
 1098 photochemical ozone production over Central East China in June 2006: a box model analysis
 1099 using comprehensive measurements of ozone precursors, *Atmos. Chem. Phys.*, 9, 7711-7723,
 1100 <https://doi.org/10.5194/acp-9-7711-2009>, 2009.

1101 Kanaya, Y., H. Tanimoto, Y. Yokouchi, F. Taketani, Y. Komazaki, H. Irie, H. Takashima, S.
 1102 Inomata, Diagnosis of Photochemical Ozone Production Rates and Limiting Factors in
 1103 Continental Outflow Air Masses Reaching Fukue Island, Japan: Ozone-Control Implications,
 1104 *Aerosol and Air Quality Res.*, 16, 430-441, DOI: 10.4209/aaqr.2015.04.0220, 2016.

1105 Kim, N. K., Kim, Y. P., Morino, Y., Kurokawa, J.-I., and Ohara, T., “Verification of NO_x
 1106 emission inventory over South Korea using sectoral activity data and satellite observation of
 1107 NO₂ vertical column densities,” *Atmospheric Environment*, 77, 496-508, 2013.

1108 Krotkov, N. A., McLinden, C. A., Li, C., Lamsal, L. N., Celarier, E. A., Marchenko, S. V.,
 1109 Swartz, W. H., Bucsela, E. J., Joiner, J., Duncan, B. N., Boersma, K. F., Veefkind, J. P., Levelt,
 1110 P. F., Fioletov, V. E., Dickerson, R. R., He, H., Lu, Z., and Streets, D. G. (2016), Aura OMI
 1111 observations of regional SO₂ and NO₂ pollution changes from 2005 to 2015, *Atmos. Chem.*
 1112 *Phys.*, 16, 4605-4629, <https://doi.org/10.5194/acp-16-4605-2016>.

1113 Koukouli, M. E., Theys, N., Ding, J., Zyrichidou, I., Mijling, B., Balis, D., and van der A, R. J.:
 1114 Updated SO₂ emission estimates over China using OMI/Aura observations, *Atmos. Meas. Tech.*,
 1115 11, 1817-1832, <https://doi.org/10.5194/amt-11-1817-2018>, 2018.

1116 Lahoz, W. A. & Schneider, P. (2014), Data assimilation: making sense of Earth Observation,
 1117 *Front. Environ. Sci.*, 2, 16, doi:10.3389/fenvs.2014.00016.

1118 Lee, H.-J., S.-W. Kim, J. Brioude, O. R. Cooper, G. J. Frost, C.-H. Kim, R. J. Park, M. Trainer,
 1119 and J.-H. Woo (2014), Transport of NO_x in East Asia identified by satellite and in situ
 1120 measurements and Lagrangian particle dispersion model simulations, *J. Geophys. Res. Atmos.*,
 1121 119, 2574–2596, doi: 10.1002/2013JD021185.

1122 Lee, D., Lee, Y.-M., Jang, K.-W., Yoo, C., Kang, K.-H., Lee, J.-H., Jung, S.-W., Park, J.-M.,
 1123 Lee, S.-B., Han, J.- S., Hong, J.-H., & Lee, S.-J. (2011), Korean National Emissions Inventory
 1124 System and 2007 Air Pollutant Emissions, *Asian Journal of Atmospheric Environment*, 5, 278–
 1125 291, <https://doi.org/10.5572/ajae.2011.5.4.278>.

1126 Levelt, P. F., Hilsenrath, E., Leppelmeier, G. W., van den Oord, G. H. J., Bhartia, P. K.,
 1127 Tamminen, J., de Haan, J. F., & Veefkind, J. P. (2006), Science objectives of the Ozone
 1128 Monitoring Instrument, *Geosci. Remote Sens.*, 44, 1199–1208.

1129 Levelt P.F., Joiner J., Tamminen J., Veefkind J.P., Bhartia P.K., Stein Zweers D.C., Duncan
 1130 B.N., Streets D.G., Eskes H., van der A R., McLinden C., Fioletov V., Carn S., de Laat J.,
 1131 DeLand M., Marchenko S., McPeters R., Ziemke J., Fu D., Liu X., Pickering K., Apituley A.,
 1132 González Abad G., Arola A., Boersma F., Chan Miller C., Chance K., de Graaf M., Hakkarainen
 1133 J., Hassinen S., Ialongo I., Kleipool Q., Krotkov N., Li C., Lamsal L., Newman P., Nowlan C.,
 1134 Suleiman R., Tilstra L. G., Torres O., Wang H., and Wargan K.: The Ozone Monitoring
 1135 Instrument: overview of 14 years in space, *Atmos. Chem. Phys.*, 18, 5,699-5,745,
 1136 <https://doi.org/10.5194/acp-18-5699-2018>, 2018.

1137 Li, C., Joiner, J., Krotkov, N. A. & Bhartia, P. K. (2013), A fast and sensitive new satellite SO₂
 1138 retrieval algorithm based on principal component analysis: Application to the ozone monitoring
 1139 instrument, *Geophys. Res. Lett.*, 40(23), 6314–6318, doi:10.1002/2013GL058134.

1140 Li, C., C. McLinden, V. Fioletov, N.A. Krotkov, S.A. Carn, J. Joiner, D. Streets, H. He, X. Ren,
 1141 Z. Li, & R.R. Dickerson (2017), India is overtaking China as the world's largest emitter of
 1142 anthropogenic sulfur dioxide, *Sci. Rep.*, 7, 14304, doi:10.1038/s41598-017-14639-8.

1143 Ling, Z., Huang, T., Zhao, Y., Li, J., Zhang, X., Wang, J., Lian, L., Mao, X., Gao, H., & Ma, J.
 1144 (2017), OMI-measured increasing SO₂ emissions due to energy industry expansion and
 1145 relocation in northwestern China, *Atmos. Chem. Phys.*, 17, 9115-9131,
 1146 <https://doi.org/10.5194/acp-17-9115-2017>.

1147 Liu, F., Beirle, S., Zhang, Q., van der A, R. J., Zheng, B., Tong, D., & He, K. (2017), NO_x
 1148 emission trends over Chinese cities estimated from OMI observations during 2005 to 2015,
 1149 *Atmos. Chem. Phys.*, 17, 9261-9275, <https://doi.org/10.5194/acp-17-9261-2017>.

1150 Livesey, N. J., Read, W. G., Froidevaux, L., Lambert, A., Manney, G. L., Pumphrey, H. C.,
 1151 Santee, M. L., Schwartz, M. J., Wang, S., Cofield, R. E., Cuddy, D. T., Fuller, R. A., Jarnot, R.
 1152 F., Jiang, J. H., Knosp, B. W., Stek, P. C., Wagner, P. A., and Wu, D. L. (2011), Aura
 1153 Microwave Limb Sounder (MLS), Version 3.3 Level 2 data quality and description document,
 1154 Tech. Rep. JPL D-33509, Jet Propul. Lab., Pasadena, CA.

1155 Luo M., Read W., Kulawik S., Worden J., Livesey N., Bowman K., and Herman R., Carbon
 1156 monoxide (CO) vertical profiles derived from joined TES and MLS measurements, *Journal Of*
 1157 *Geophysical Research*, VOL. 118, 1–13, doi:10.1002/jgrd.50800, 2013, August 29, 2013.

1158 Mao, J., Fan, S., Jacob, D.J., and Travis, K. R.: Radical loss in the atmosphere from Cu-Fe redox
 1159 coupling in aerosols, *Atmos. Chem. phys.* 13, 509-519, 2013.

1160 Mijling, B., van der A, R. J., and Zhang, Q.: Regional nitrogen oxides emission trends in East
 1161 Asia observed from space, *Atmos. Chem. Phys.*, 13, 12003-12012, [https://doi.org/10.5194/acp-](https://doi.org/10.5194/acp-13-12003-2013)
 1162 13-12003-2013, 2013.

1163 Millet, D. B., D. J. Jacob, K. F. Boersma, T. M. Fu, T. P. Kurosu, K. Chance, C. L. Heald, & A.
 1164 Guenther (2008), Spatial distribution of isoprene emissions from North America derived from
 1165 formaldehyde column measurements by the OMI satellite sensor, *J. Geophys. Res.*, 113, D02307,
 1166 doi:10.1029/2007JD008950.

1167 Miyazaki, K., Eskes, H. J., & Sudo, K. (2012a), Global NO_x emission estimates derived from an
 1168 assimilation of OMI tropospheric NO₂ columns, *Atmospheric Chemistry and Physics*, 12, 2263-
 1169 2288, doi:10.5194/acp-12-2263-2012.

1170 Miyazaki, K., Eskes, H. J., Sudo, K., Takigawa, M., van Weele, M., & Boersma, K. F. (2012b),
 1171 Simultaneous assimilation of satellite NO₂, O₃, CO, and HNO₃ data for the analysis of
 1172 tropospheric chemical composition and emissions, *Atmospheric Chemistry and Physics*, 12,
 1173 9545-9579, doi:10.5194/acp-12-9545-2012.

1174 Miyazaki, K., & H. Eskes (2013), Constraints on surface NO_x emissions by assimilating
 1175 satellite observations of multiple species, *Geophysical Research Letter*, 40,
 1176 doi:10.1002/grl.50894.

1177 Miyazaki, K., H. Eskes, K. Sudo, & C. Zhang (2014), Global lightning NO_x production
 1178 estimated by an assimilation of multiple satellite datasets, *Atmospheric Chemistry and*
 1179 *Physics*, 14, 3277-3305.

1180 Miyazaki, K., Eskes, H. J., & Sudo, K. (2015), A tropospheric chemistry reanalysis for the years
 1181 2005–2012 based on an assimilation of OMI, MLS, TES, and MOPITT satellite data, *Atmos.*
 1182 *Chem. Phys.*, 15, 8315-8348, doi:10.5194/acp-15-8315-2015.

1183 Miyazaki, K. & Bowman, K. (2017), Evaluation of ACCMIP ozone simulations and ozonesonde
 1184 sampling biases using a satellite-based multi-constituent chemical reanalysis, *Atmos. Chem.*
 1185 *Phys.*, 17, 8285-8312, <https://doi.org/10.5194/acp-17-8285-2017>.

1186 Miyazaki, K., Eskes, H., Sudo, K., Boersma, K. F., Bowman, K., & Kanaya, Y. (2017), Decadal
 1187 changes in global surface NO_x emissions from multi-constituent satellite data assimilation,
 1188 *Atmos. Chem. Phys.*, 17, 807-837, doi:10.5194/acp-17-807-2017.

1189 Morgenstern, O., Hegglin, M. I., Rozanov, E., O'Connor, F. M., Abraham, N. L., Akiyoshi, H.,
 1190 Archibald, A. T., Bekki, S., Butchart, N., Chipperfield, M. P., Deushi, M., Dhomse, S. S.,
 1191 Garcia, R. R., Hardiman, S. C., Horowitz, L. W., Jöckel, P., Josse, B., Kinnison, D., Lin, M.,
 1192 Mancini, E., Manyin, M. E., Marchand, M., Marécal, V., Michou, M., Oman, L. D., Pitari, G.,
 1193 Plummer, D. A., Revell, L. E., Saint-Martin, D., Schofield, R., Stenke, A., Stone, K., Sudo, K.,
 1194 Tanaka, T. Y., Tilmes, S., Yamashita, Y., Yoshida, K., and Zeng, G. (2017), Review of the
 1195 global models used within phase 1 of the Chemistry–Climate Model Initiative (CCMI), *Geosci.*
 1196 *Model Dev.*, 10, 639-671, <https://doi.org/10.5194/gmd-10-639-2017>.

1197 Myhre, G., Shindell, D., Bréon, F.-M., Collins, W., Fuglestad, J., Huang, J., Koch, D.,
 1198 Lamarque, J.-F., Lee, D., Mendoza, B., Nakajima, T., Robock, A., Stephens, G., Takemura, T.,
 1199 & Zhang, H.: Anthropogenic and Natural Radiative Forcing, in: Climate Change 2013 (2013),

1200 The Physical Science Basis. Contribution of Working Group I to the Fifth Assessment Report of
 1201 the Inter-governmental Panel on Climate Change, edited by: Stocker, T. F., Qin, D., Plattner, G.-
 1202 K., Tignor, M., Allen, S. K., Boschung, J., Nauels, A., Xia, Y., Bex, V., and Midgley, P. M.,
 1203 Cambridge University Press, Cambridge, UK and New York, NY, USA.

1204 Na K., Moon K. & Kim Y. P. (2005), Source contribution to aromatic VOC concentration and
 1205 ozone formation potential in the atmosphere of Seoul. *Atmos. Environ.* 39, 5517–5524.

1206 Oikawa, P. Y., Ge, C., Wang, J., Eberwein, J. R., Liang, L. L., Allsman, L. A., Grantz, D. A., &
 1207 Jenerette, G. D. (2015), Unusually high soil nitrogen oxide emissions influence air quality in a
 1208 high-temperature agricultural region, *Nat. Commun.*, 6, 8753, doi:10.1038/ncomms9753.

1209 Parrington, M., Jones, D. B. A., Bowman, K. W., Thompson, A. M., Tarasick, D. W., Merrill, J.,
 1210 Oltmans, S. J., Leblanc, T., Witte, J. C., & Millet, D. B. (2009), Impact of the assimilation of
 1211 ozone from the Tropospheric Emission Spectrometer on surface ozone across North America,
 1212 *Geophys. Res. Lett.*, 36, L04802, <https://doi.org/10.1029/2008GL036935>.

1213 Price, C., and D. Rind (1992), A simple lightning parameterization for calculating global
 1214 lightning distributions. *J. Geophys. Res.*, 97, 9919–9933, doi:10.1029/92JD00719.

1215 Qu, Z., D. K. Henze, S. L. Capps, Y. Wang, X. Xu, J. Wang, and M. Keller, (2017), Monthly
 1216 top-down NO_x emissions for China (2005–2012): A hybrid inversion method and trend analysis,
 1217 *J. Geophys. Res. Atmos.*, 122, 4600–4625, doi: 10.1002/2016JD025852.

1218 Randerson, J.T., G.R. van der Werf, L. Giglio, G.J. Collatz, and P.S. Kasibhatla. 2018. Global
 1219 Fire Emissions Database, Version 4, (GFEDv4). ORNL DAAC, Oak Ridge, Tennessee,
 1220 USA. <https://doi.org/10.3334/ORNLDAAAC/1293>

1221 Reuter, M., Buchwitz, M., Hilboll, A., Richter, A., Schneising, O., Hilker, M., Heymann, J.,
 1222 Bovensmann, H., & Burrows, J. P. (2014), Decreasing emissions of NO_x relative to CO₂ in East
 1223 Asia inferred from satellite observations, *Nat. Geosci.*, 7, 792–795, doi:10.1038/ngeo2257.

1224 Richter, A. & Burrows, J. P. (2002), Tropospheric NO₂ from GOME measurements, *Adv. Space*
 1225 *Res.*, 29 (11), 1673–1683.

1226 Sekiya, T., Miyazaki, K., Ogochi, K., Sudo, K., & Takigawa, M. (2018), Global high-resolution
 1227 simulations of tropospheric nitrogen dioxide using CHASER V4.0, *Geosci. Model Dev.*,
 1228 <https://doi.org/10.5194/gmd-2017-203>, in press.

1229 Stevenson, D. S., Young, P. J., Naik, V., Lamarque, J.-F., Shindell, D. T., Voulgarakis, A.,
 1230 Skeie, R. B., Dalsoren, S. B., Myhre, G., Berntsen, T. K., Folberth, G. A., Rumbold, S. T.,
 1231 Collins, W. J., MacKenzie, I. A., Doherty, R. M., Zeng, G., van Noije, T. P. C., Strunk, A.,
 1232 Bergmann, D., Cameron-Smith, P., Plummer, D. A., Strode, S. A., Horowitz, L., Lee, Y. H.,
 1233 Szopa, S., Sudo, K., Nagashima, T., Josse, B., Cionni, I., Righi, M., Eyring, V., Conley, A.,
 1234 Bowman, K. W., Wild, O., & Archibald, A. (2013), Tropospheric ozone changes, radiative
 1235 forcing and attribution to emissions in the Atmospheric Chemistry and Climate Model

1236 Intercomparison Project (ACCMIP), *Atmos. Chem. Phys.*, 13, 3063–3085,
1237 <https://doi.org/10.5194/acp-13-3063-2013>.

1238 Strode, S. A., Worden, H. M., Damon, M., Douglass, A. R., Duncan, B. N., Emmons, L. K.,
1239 Lamarque, J.-F., Manyin, M., Oman, L. D., Rodriguez, J. M., Strahan, S. E., & Tilmes, S.
1240 (2016), Interpreting space-based trends in carbon monoxide with multiple models, *Atmos. Chem.*
1241 *Phys.*, 16, 7285–7294, <https://doi.org/10.5194/acp-16-7285-2016>.

1242 Tang, W., Arellano, A. F., DiGangi, J. P., Choi, Y., Diskin, G. S., Agustí-Panareda, A.,
1243 Parrington, M., Massart, S., Gaubert, B., Lee, Y., Kim, D., Jung, J., Hong, J., Hong, J.-W.,
1244 Kanaya, Y., Lee, M., Stauffer, R. M., Thompson, A. M., Flynn, J. H., and Woo, J.-H.: Evaluating
1245 high-resolution forecasts of atmospheric CO and CO₂ from a global prediction system during
1246 KORUS-AQ field campaign, *Atmos. Chem. Phys.*, 18, 11007–11030,
1247 <https://doi.org/10.5194/acp-18-11007-2018>, 2018.

1248 Thornton, J. A., P. J. Wooldridge, & R. C. Cohen (2000), Atmospheric NO₂: In Situ Laser-
1249 Induced Fluorescence Detection at Parts per Trillion Mixing Ratios, *Anal. Chem.*, 72, 528–539.

1250 Valin, L. C., Russell, A. R., Hudman, R. C., & Cohen, R. C. (2011), Effects of model resolution
1251 on the interpretation of satellite NO₂ observations, *Atmos. Chem. Phys.*, 11, 11647–11655,
1252 <https://doi.org/10.5194/acp-11-11647-2011>.

1253 van der A, R. J., Mijling, B., Ding, J., Koukouli, M. E., Liu, F., Li, Q., Mao, H., & Theys, N.
1254 (2017), Cleaning up the air: effectiveness of air quality policy for SO₂ and NO_x emissions in
1255 China, *Atmos. Chem. Phys.*, 17, 1775–1789, <https://doi.org/10.5194/acp-17-1775-2017>.

1256 van der Werf, G. R., Randerson, J. T., Giglio, J., Mu, M., Kasibhatla, P. S., Morton, D. C., Jin,
1257 Y., & van Leeuwen, T. T. (2010), Global fire emissions and the contribution of deforestation,
1258 savanna, forest, agricultural, and peat fires (1997–2009), *Atmos. Chem. Phys.*, 10, 11707–11735,
1259 <https://doi.org/10.5194/acp-10-11707-2010>.

1260 van Donkelaar, A., Martin, R. V., Leaitch, W. R., Macdonald, A. M., Walker, T. W., Streets, D.
1261 G., Zhang, Q., Dunlea, E. J., Jimenez, J. L., Dibb, J. E., Huey, L. G., Weber, R., and Andreae, M.
1262 O. (2008), Analysis of aircraft and satellite measurements from the Intercontinental Chemical
1263 Transport Experiment (INTEX-B) to quantify long-range transport of East Asian sulfur to
1264 Canada, *Atmos. Chem. Phys.*, 8, 2999–3014, doi:10.5194/acp-8-2999-2008.

1265 Verstraeten, W. W., Neu, J. L., Williams, J. E., Bowman, K. W., Worden, J. R., & Boersma, K.
1266 F. (2015), Rapid increases in tropospheric ozone production and export from China, *Nat.*
1267 *Geosci.*, 8, 690–695, <https://doi.org/10.1038/ngeo2493>.

1268 Yienger, J. J. and Levy II, H. (1995), Empirical model of global soil biogenic NO_x emissions, *J.*
1269 *Geophys. Res.*, 100, 11447–11464.

1270 van der A, R. J., Mijling, B., Ding, J., Koukouli, M. E., Liu, F., Li, Q., Mao, H., and Theys, N.:
 1271 Cleaning up the air: effectiveness of air quality policy for SO₂ and NO_x emissions in China,
 1272 *Atmos. Chem. Phys.*, 17, 1775-1789, <https://doi.org/10.5194/acp-17-1775-2017>, 2017.

1273 Vinken, G. C. M., Boersma, K. F., Maasakkers, J. D., Adon, M., & Martin, R. V. (2014),
 1274 Worldwide biogenic soil NO_x emissions inferred from OMI NO₂ observations, *Atmos. Chem.*
 1275 *Phys.*, 14, 10363– 10381, doi:10.5194/acp-14-10363-2014.

1276 Warner, J. X., Wei, Z., Strow, L. L., Barnet, C. D., Sparling, L. C., Diskin, G., & Sachse, G.
 1277 (2010), Improved agreement of AIRS tropospheric carbon monoxide products with other EOS
 1278 sensors using optimal estimation retrievals, *Atmos. Chem. Phys.*, 10, 9521-9533,
 1279 <https://doi.org/10.5194/acp-10-9521-2010>.

1280 Wang, Y., Jacob, D. J., and Logan, J. A. (1998), Global simulation of tropospheric O₃-NO_x-
 1281 hydrocarbon chemistry: 1. Model formulation, *J. Geophys. Res.*, 103, 10713-10725.

1282 Wang, S. & J. Hao (2012) Air Quality Management in China: Issues, Challenges, and Options.
 1283 *Journal of Environmental Sciences* 24: 2–13.

1284 Wang, S. W., Q. Zhang, R. V. Martin, S. Philip, F. Liu, M. Li, X. J. Jiang, and K. B. He (2015),
 1285 Satellite measurements oversee China's sulfur dioxide emission reductions from coal-fired
 1286 power plants, *Environ. Res. Letts.*, 10, 114015.

1287 Watanabe, S., Hajima, T., Sudo, K., Nagashima, T., Takemura, T., Okajima, H., Nozawa, T.,
 1288 Kawase, H., Abe, M., Yokohata, T., Ise, T., Sato, H., Kato, E., Takata, K., Emori, S., &
 1289 Kawamiya, M. (2011), MIROC-ESM 2010: model description and basic results of CMIP5-
 1290 20c3m experiments, *Geosci. Model Dev.*, 4, 845–872, <https://doi.org/10.5194/gmd-4-845-2011>.

1291 Weibring, P., D. Richter, J. G. Walega, & A. Friedet (2007), First Demonstration of a High
 1292 Performance Difference Frequency Spectrometer on Airborne Platforms, *Optics Express*, 15,
 1293 13476-13495.

1294 Weinheimer, A. J., Walega, J. G., Ridley, B. A., Sachse, G. W., Anderson, B. E., & Collins, J. E.
 1295 (1993), Stratospheric NO_y measurements on the NASA DC-8 during AASE-II, *Geophys. Res.*
 1296 *Lett.*, 20, 2563–2566.

1297 Woo, J.-H., Choi, K.-C., Kim, H.K., Baek, B.H., Jang, M., Eum, J.-H., Song, C.H., Ma, Y.-I.,
 1298 Sunwoo, Y., Chang, L.-S., Yoo, S.H. (2012) Development of an anthropogenic emissions
 1299 processing system for Asia using SMOKE. *Atmospheric Environment* 58, 5-13.

1300 Worden, H.M., Edwards, D.P., Deeter, M.N., Fu, D., Kulawik, S.S., Worden, J.R., Arellano, A.,
 1301 (2013), Averaging kernel prediction from atmospheric and surface state parameters based on
 1302 multiple regression for nadir-viewing satellite measurements of carbon monoxide and ozone,”
 1303 *Atmos. Meas. Tech.*, 6, 1633–1646.

1304 Zhang, Q., Streets, D. G., Carmichael, G. R., He, K. B., Huo, H., Kannari, A., Klimont, Z., Park,
1305 I. S., Reddy, S., Fu, J. S., Chen, D., Duan, L., Lei, Y., Wang, L. T., & Yao, Z. L. (2009), Asian
1306 emissions in 2006 for the NASA INTEx-B mission, *Atmos. Chem. Phys.*, 9, 5131-5153.

1307

1308

Figure 1. Comparison of mean vertical ozone profiles (in ppbv) between observations (black), model (blue), and reanalysis (red) averaged over the KORUS-AQ period. Top row shows mean profile; middle and bottom rows show mean difference and root-mean-square-error (RMSE) between model simulation and observations (blue) and between the reanalysis and the observations (red), respectively. From left to right, results are shown for DC-8 aircraft measurements over the Seoul Metropolitan Area (SMA), outside of the SMA, and ozonesonde measurements at Taehwa and Olympic Park.

Figure 2. Spatial distribution of mean ozone concentrations (in ppbv) averaged over the campaign period from a DC-8 aircraft sampling between the surface and 800 hPa (top), 800 and 500 hPa (middle), and 500 and 100 hPa (bottom). From left to right, results are shown for DC-8 aircraft measurements, model, reanalysis, mean difference between the model and the observations, and mean difference between the reanalysis and the observations. The black square line represents the SMA region (defined as 36.6°N–37.9°N, 126.4°E–127.6°E in this study).

Figure 3. Spatial distribution of ozone (in ppbv) at 850 hPa on May 25, 2016 from the reanalysis (left), and its changes due to Chinese NO_x emissions (right). The impacts of Chinese NO_x emissions were measured by comparing the results from a control model simulation (using the optimized emission from data assimilation) and sensitivity model simulations using modified NO_x emissions where the emissions in China were set to zero. Vectors represent horizontal winds obtained from the GCM calculation nudged to ERA-Interim.

Figure 4. Spatial distribution in mean ozone concentrations (in ppbv) from the reanalysis at 700 hPa averaged during (a) 1–16 May 2016 (phase 1), (b) 17–22 May 2016 (phase 2), (c) 25–31 May 2016 (phase 3), and (d) 1–6 June 2016 (phase 4). Vectors represent horizontal winds obtained from the GCM calculation nudged to ERA-Interim.

Figure 5. Same as in Figure 1 but for DC-8 measurements over the SMA (top) and outside of the SMA (bottom) averaged during the individual phases (from left to right, phases 1 to 4). Error bars represent the standard deviation of all data within each bin.

Figure 6. Spatial distribution of mean analysis spread (in ppbv, shaded) and mean ozone concentration (in ppbv, contour) from the reanalysis at 700 hPa averaged during the individual phases (from left to right, phases 1 to 4) for the reanalysis calculation.

Figure 7. Comparison of mean vertical profile between observations (black), model (blue), and reanalysis (red) for CO (ppbv), HNO₃ (ppbv), SO₂ (ppbv), NO₂ (pptv), NO (pptv), OH (pptv), H₂O (ppbv), HO₂ (pptv), CH₂O (pptv), and PAN (pptv) averaged over the KORUS-AQ period. Results are shown for the profile (a) over and (b) outside of the SMA.

Figure 8. Spatial distributions of tropospheric NO₂ column (in 10¹⁵ molecules cm⁻²) from the QA4ECV OMI retrievals (upper left), model (upper center), and reanalysis (upper right). The

lower panels show the difference between the assimilation and model simulation (left), between the model simulation and the satellite retrievals (center), and between the data assimilation and the satellite retrievals (right).

Figure 9. Spatial distributions of differences in the mean ozone concentrations (in ppbv) between the NO₂ assimilation and model at 700 hPa averaged during individual phases.

Figure 10. Absolute values of mean ozone bias (ppbv) relative to the DC-8 aircraft measurements over SMA for individual phases for the model calculation (blue), OMI and GOME-2 NO₂ assimilation (green), MOPITT CO data assimilation (orange), MLS O₃ and HNO₃ assimilation (purple), and reanalysis (red) at 400 hPa (upper panel) and 700 hPa (lower panel).

Figure 11. Comparison of mean ozone concentrations between the AIRS/OMI retrievals (left columns), model (second left columns), reanalysis (third left columns), and AIRS/OMI assimilation (right columns) at 510 hPa in May 2016. Upper row shows ozone concentrations for the global product (GL), second row shows the difference between the model simulation or assimilation and the satellite retrievals for GL; third row shows ozone concentrations for the regional product (RE), bottom row shows the difference between the model simulation or assimilation and the satellite retrievals for RE.

Figure 12. Spatial distribution of mean analysis spread (in ppbv, shading) and mean ozone concentration (in ppbv, contours) from the reanalysis at 650 hPa averaged during individual phases (from left to right, phases 1 to 3) for the AIRS/OMI data assimilation (upper panels). Spatial distributions of ozone analysis increments (in ppbv/day) from AIRS/OMI data assimilation are also shown (lower panels). Because the OMI went into survival model on May 29 and ceased operation afterwards during the KORUS-AQ period, the spread and increments in phase 4 are not discussed.

Figure 13. Mean absolute values of ozone bias (in ppbv) relative to the DC-8 aircraft measurements at 650 hPa for individual phases for the model calculation (blue), reanalysis (red), AIRS/OMI data assimilation (green), and reanalysis with assimilating AIRS/OMI data (orange).

Figure 14. Spatial distributions of surface NO_x emissions (in 10¹¹ kgN m⁻² s⁻¹, upper panels), surface CO emissions (in 10¹⁰ kgCO m⁻² s⁻¹, middle panels), and surface SO₂ emissions (in 10¹⁰ kgS m⁻² s⁻¹, bottom row) obtained from a priori emissions (left panels), a posteriori emissions from the reanalysis (center panels), and the difference between a posteriori and a priori emissions (right panels) averaged over May 2016. The black square line represents the eastern China region (100–124°E, 21–43°N) used for the emission analysis.

Table 1. Mean values and standard deviations of ozone concentrations (in ppbv) based on data assimilation analyses averaged over the entire KORUS-AQ period and during individual phases. The results corresponding to the SMA, the KORUS-AQ domain (defined as 31.5°N–37.5°N, 123°E–132°E), and the East Asia domain (defined as 29°N–45°N, 110°E–132°E) using the DC-8 aircraft sampling and complete sampling 8-h daytime (9am to 5pm) mean chemical reanalysis fields at 700 hPa are shown.

Table 2. Comparisons of mean ozone concentrations between the model simulation (Model), the standard data assimilation calculation (Reanalysis), and AIRS/OMI only data assimilation calculation (AIRS/OMI DA) in May 2016. Shown are the mean bias (BIAS: the data assimilation minus the satellite retrievals) and the root-mean-square error (RMSE) in ppbv. From left to right, results are shown for SH mid-latitudes (15–55°S), tropics (15°S–15°N), NH mid-latitudes (15–55°N) for the global product (GL), and for the East Asia regional product (RE).

Table 3. Regional total surface emissions of NO_x (in Tg N yr⁻¹), CO emissions (in Tg CO yr⁻¹), and SO₂ (Tg SO₂ yr⁻¹) from a priori and a posteriori emissions for South Korea (125–129.5°E, 34.2–38.2°N) and eastern China (100–124°E, 21–43°N) in May 2016. The a posteriori NO_x emissions were derived using two different satellite NO₂ retrievals (QA4ECV and DOMINO2) in this study. The standard deviations of the estimated daily emissions during the analysis period are shown as the uncertainty information of the a posteriori emissions. The top-down estimates from the GlobEmission systems are also shown for NO_x and SO₂ emissions.

Figure 1.

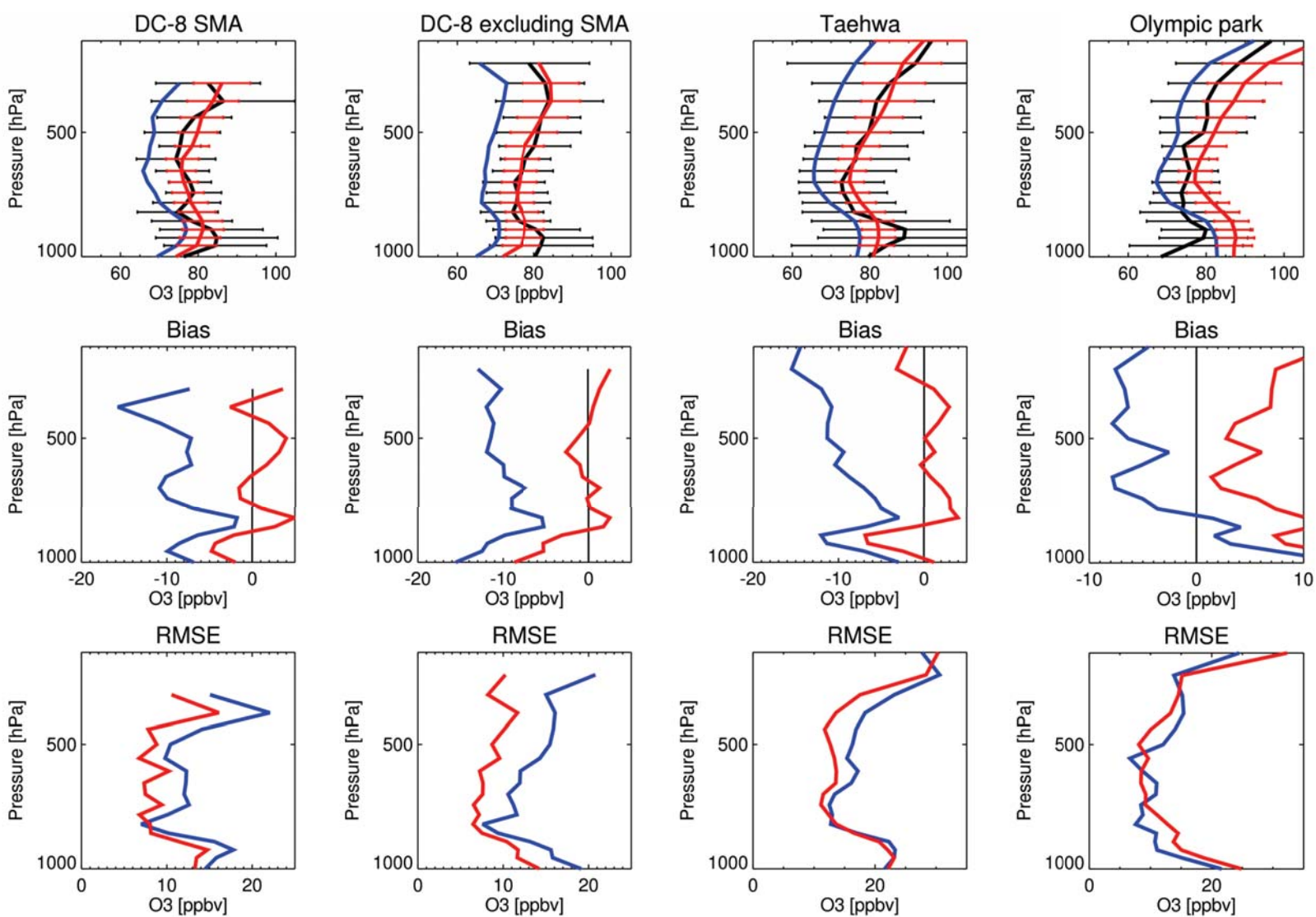


Figure 2.

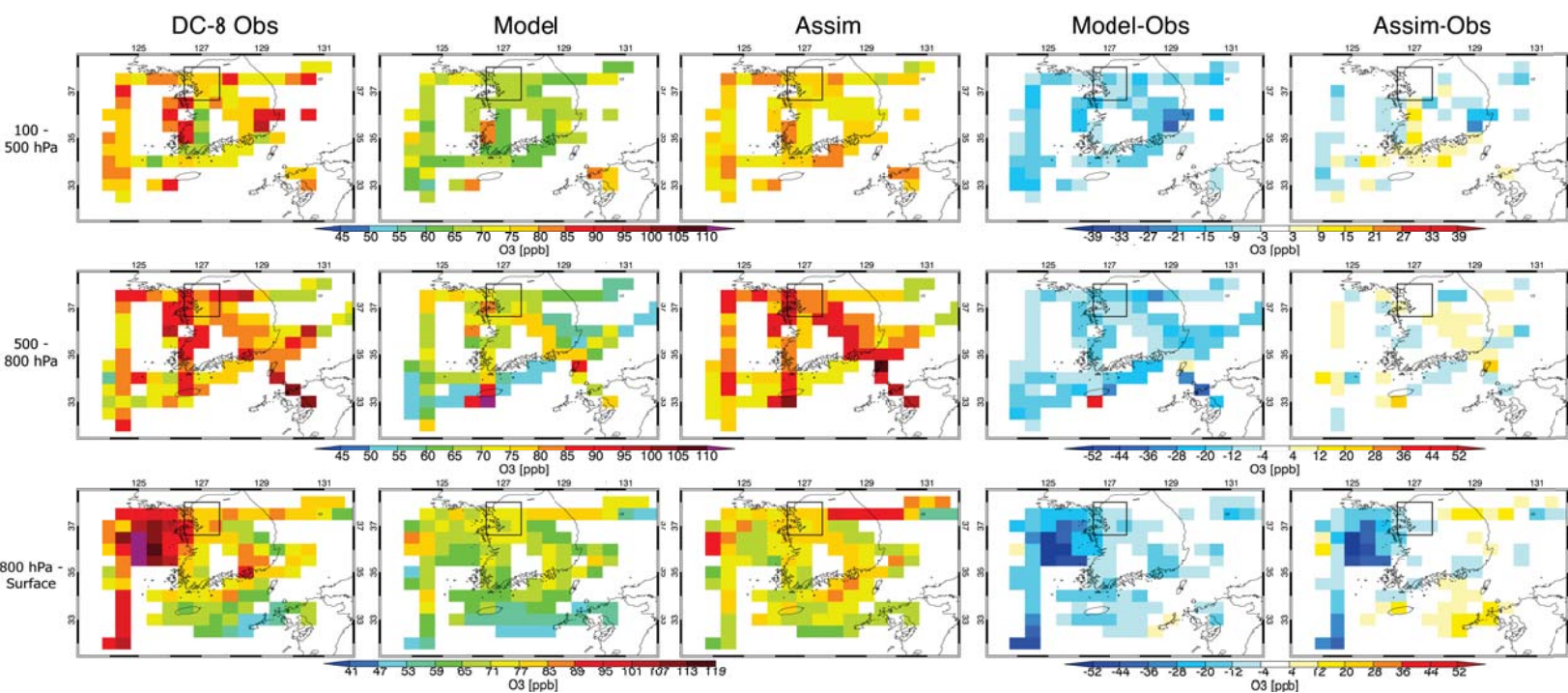
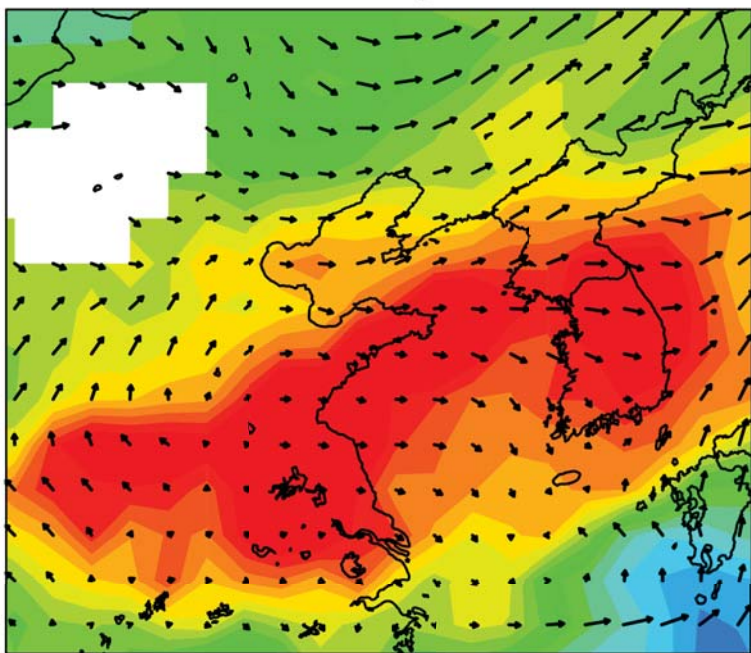


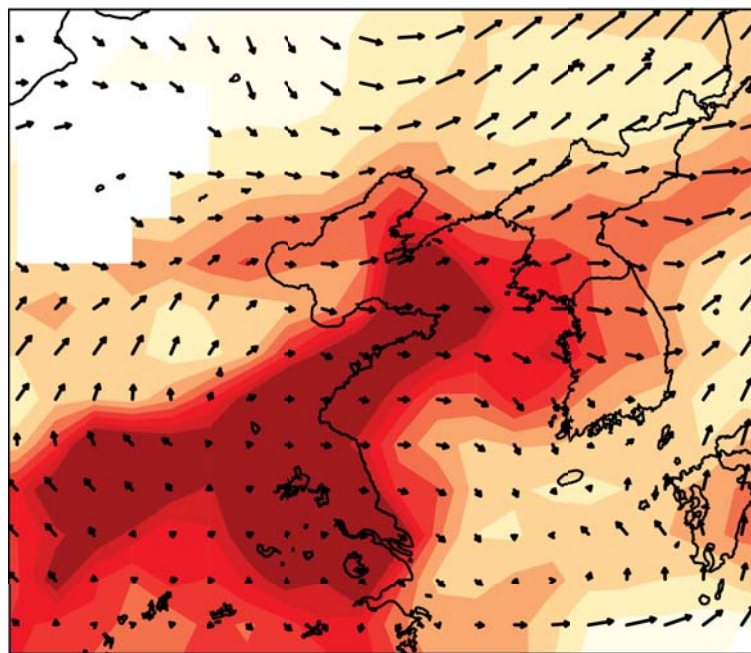
Figure 3.

Ozone on May 25, 2016



20 24 28 32 36 40 44 48 52 56 60 64 68 72 76 80 84 88 92

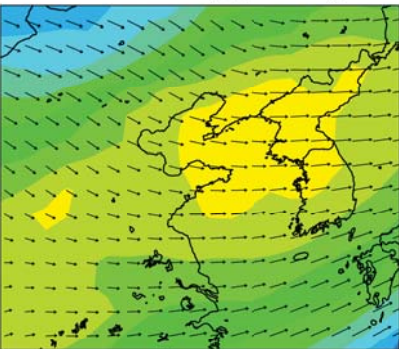
Changes due to Chinese NOx emissions



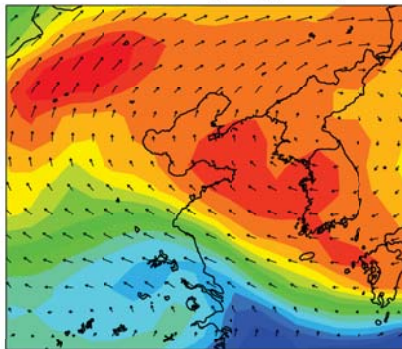
2 5 10 15 20 25 30 35 40 50

Figure 4.

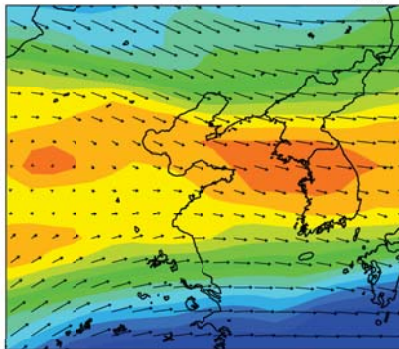
Phase 1 (dynamic)



Phase 2 (stagnant)



Phase 3 (transboundary)



Phase 4 (blocking)

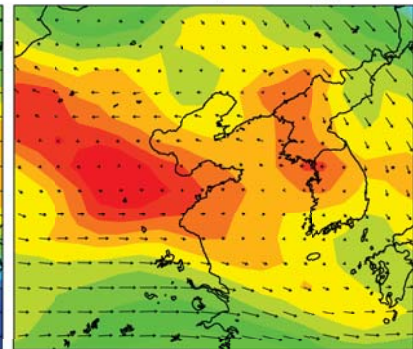


Figure 5.

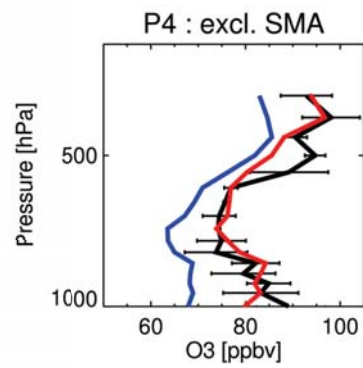
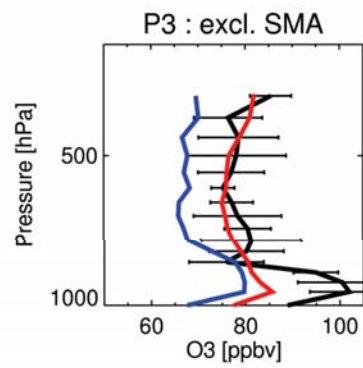
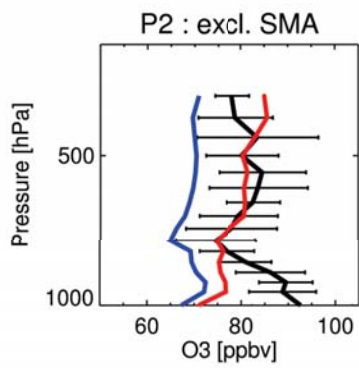
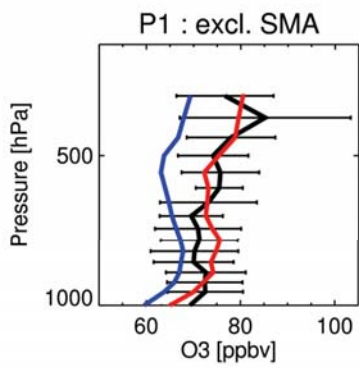
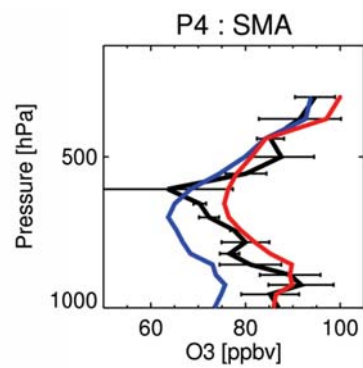
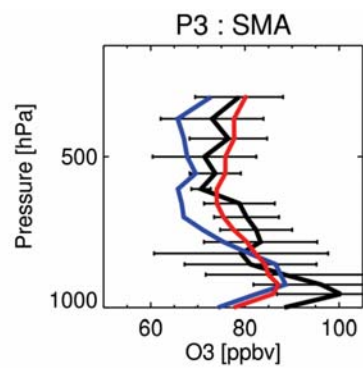
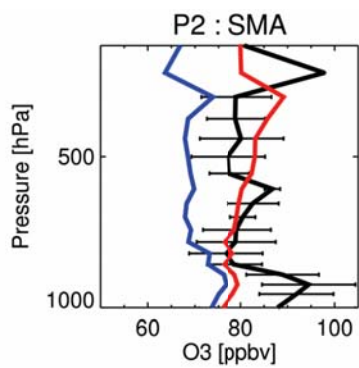
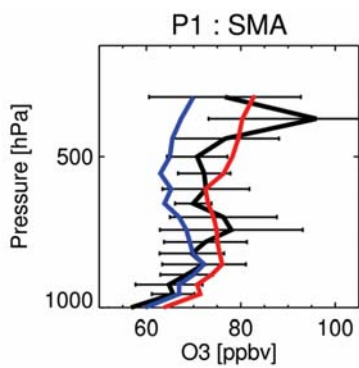
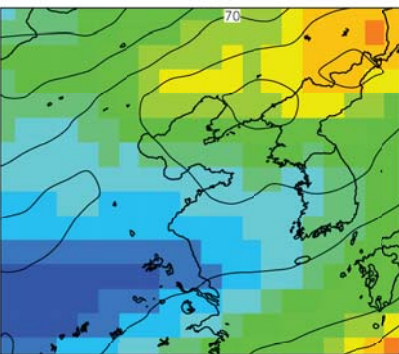
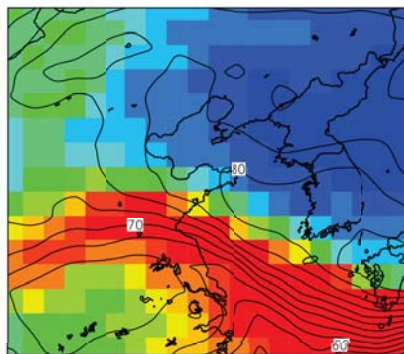


Figure 6.

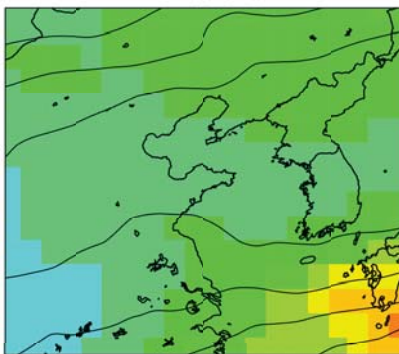
Phase 1



Phase 2



Phase 3



Phase 4

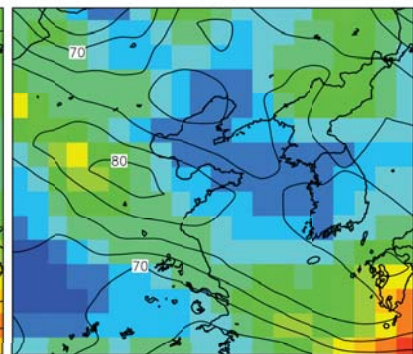
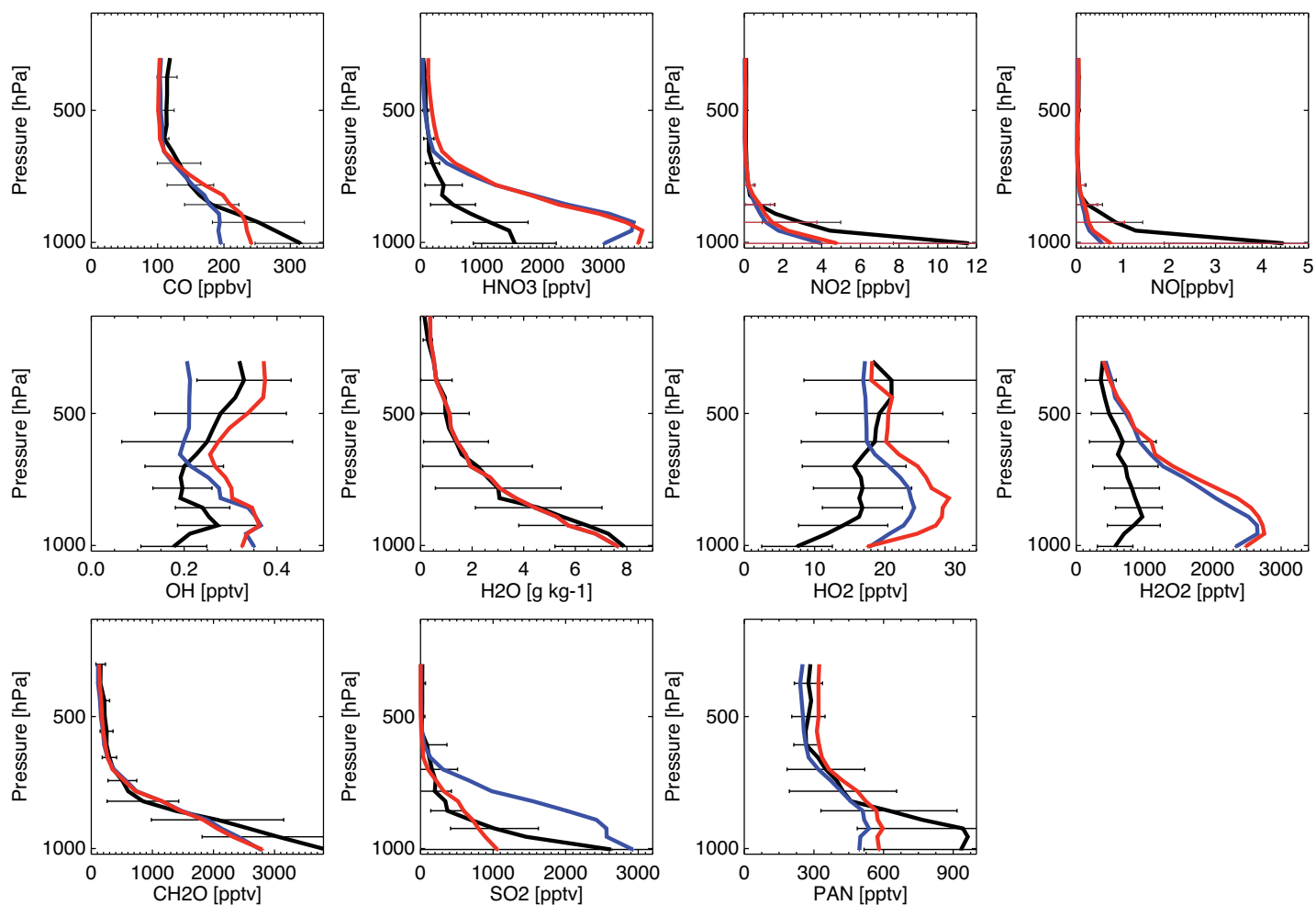


Figure 7.

(a) SMA



(b) Outside of SMA

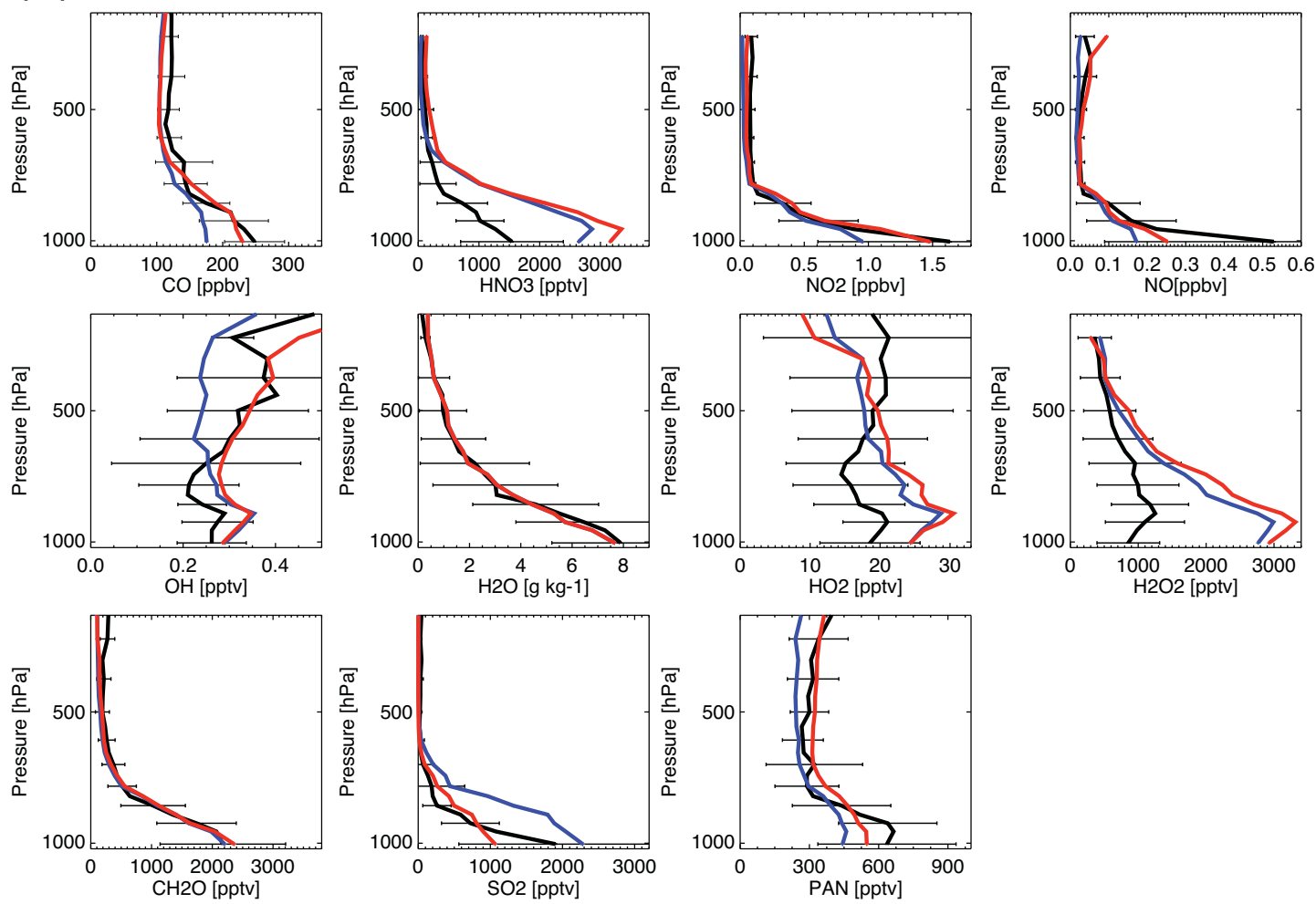
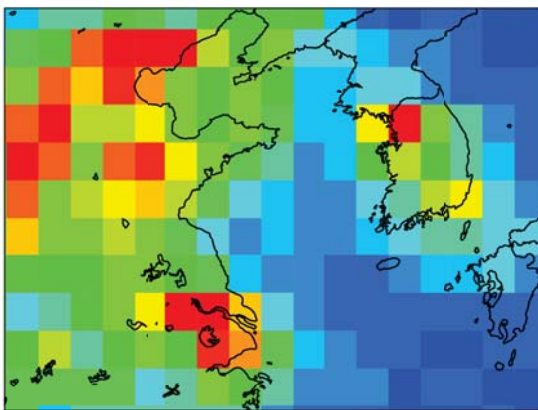
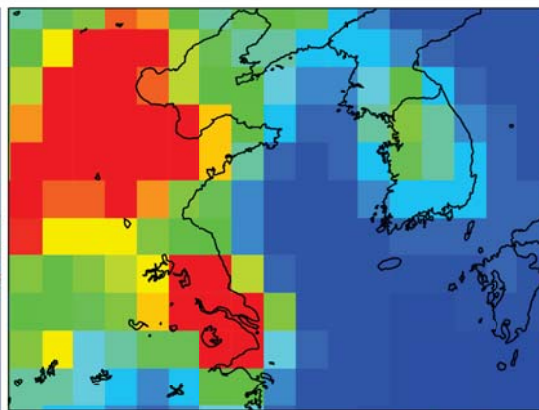


Figure 8.

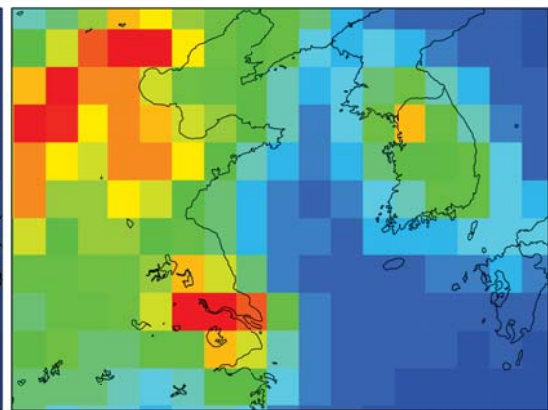
OMI NO₂ Obs



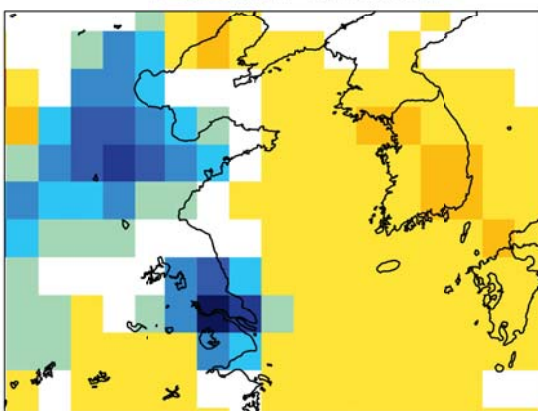
Model



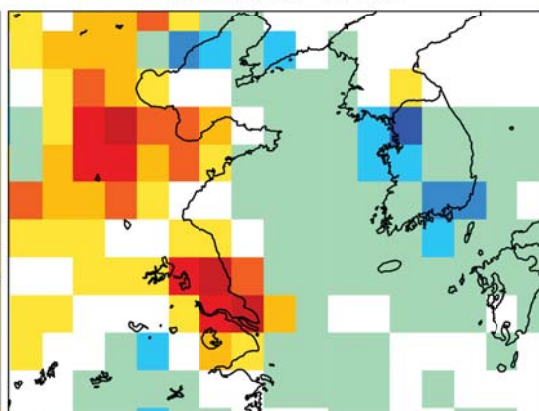
Assim



Assim-Model



Model-Obs



Assim-Obs

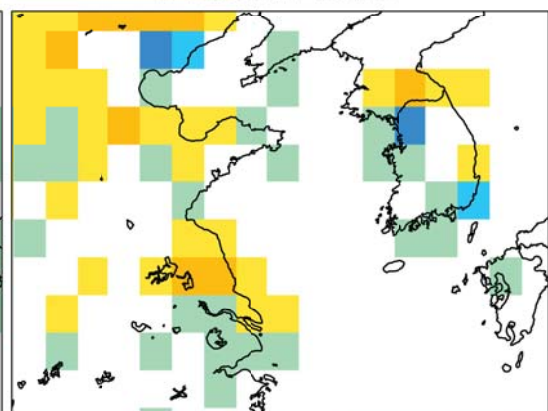
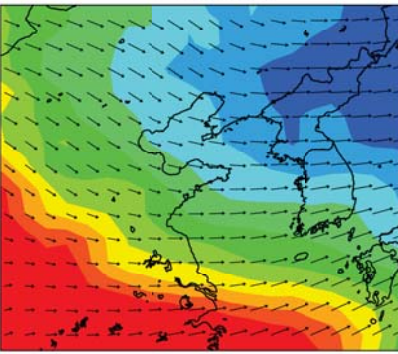


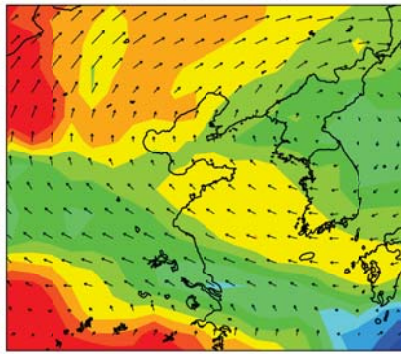
Figure 9.

Ozone at 700 hPa (NO_2 assim - Model)

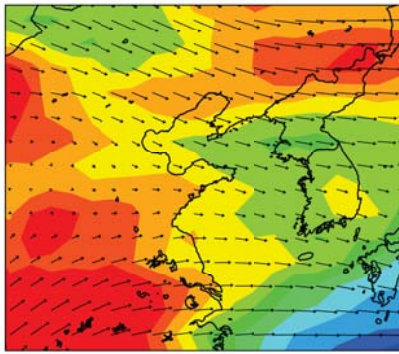
Phase 1



Phase 2



Phase 3



Phase 4

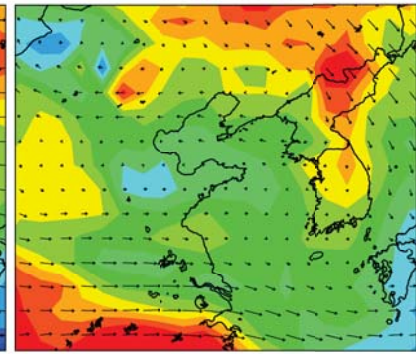
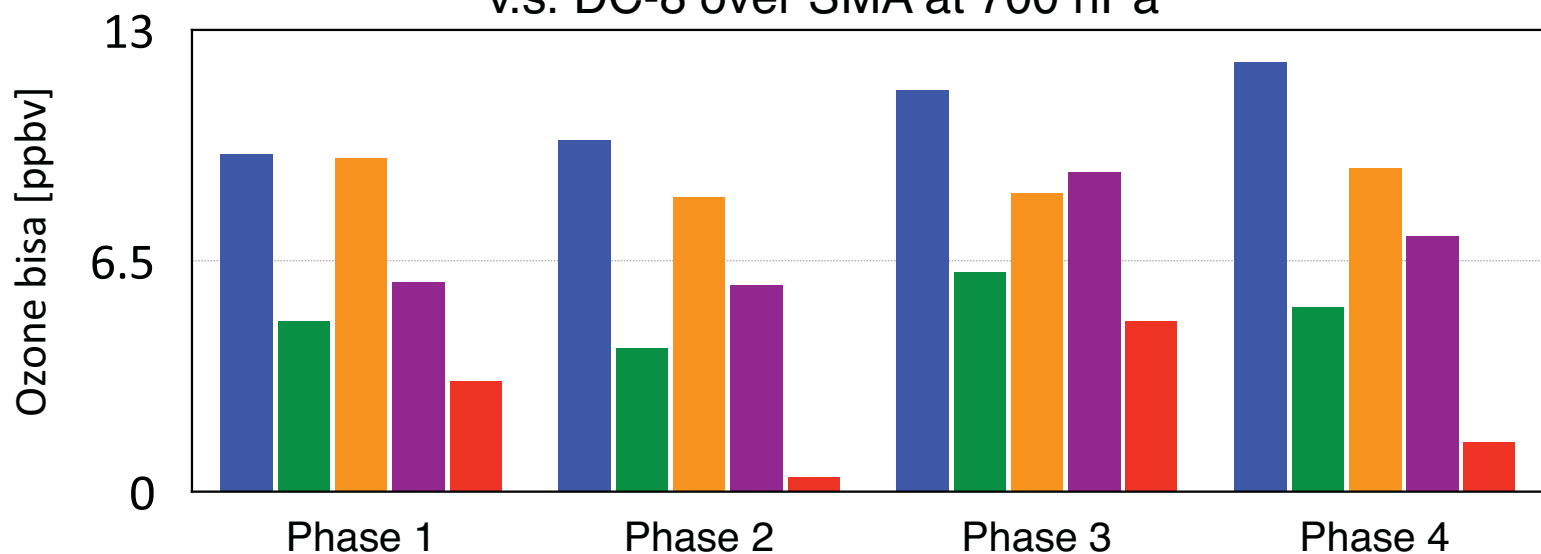


Figure 10.

v.s. DC-8 over SMA at 700 hPa



v.s. DC-8 over SMA at 400 hPa

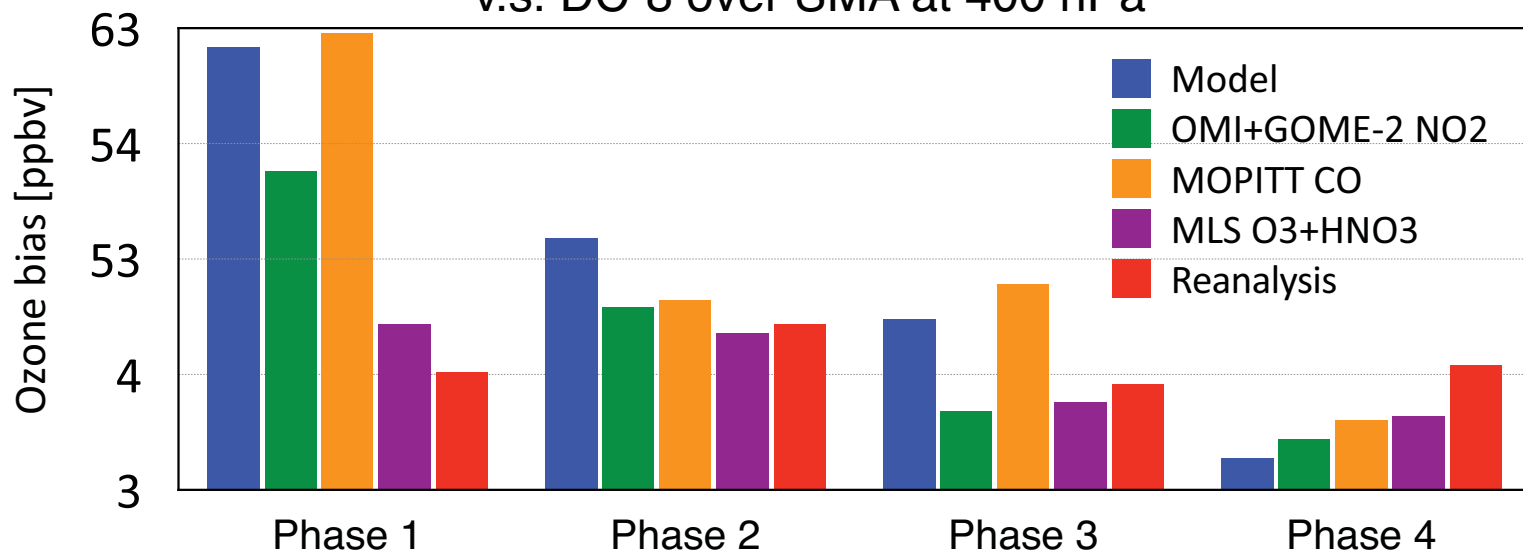


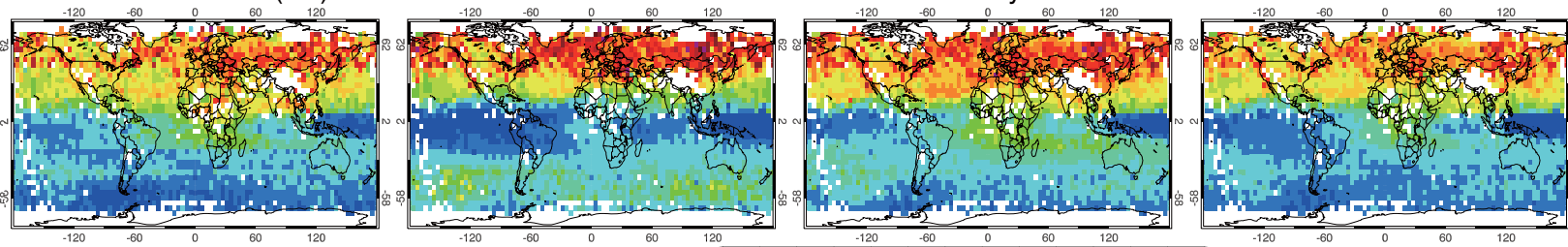
Figure 11.

AIRS/OMI Obs (GL)

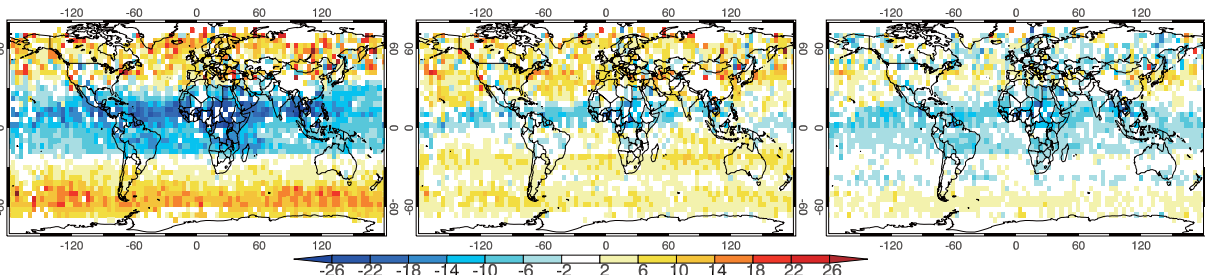
Model

Reanalysis

AIRS/OMI assim



difference
from Obs

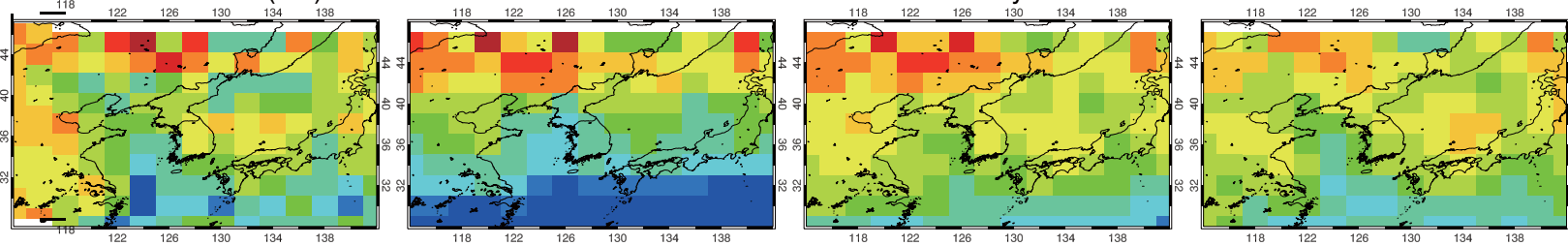


AIRS/OMI Obs (RE)

Model

Reanalysis

AIRS/OMI assim



difference
from Obs

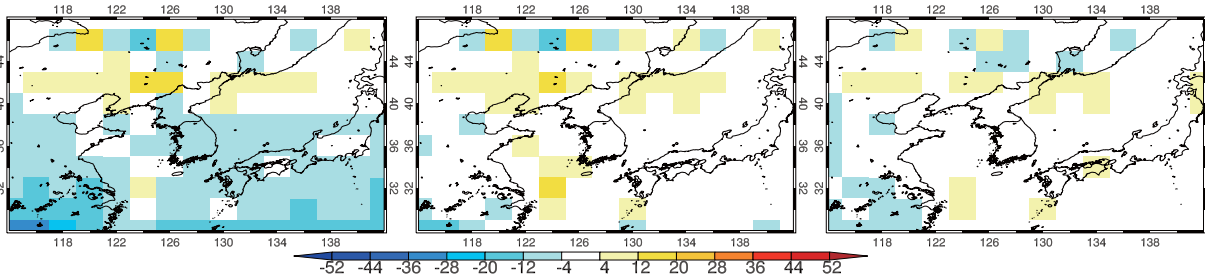


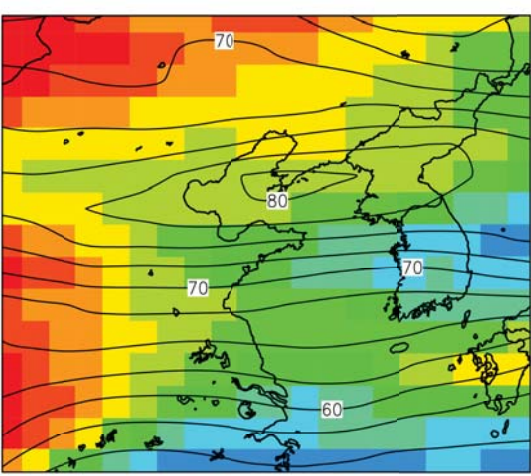
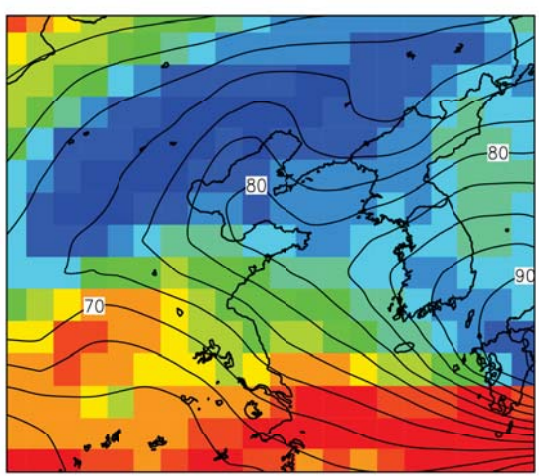
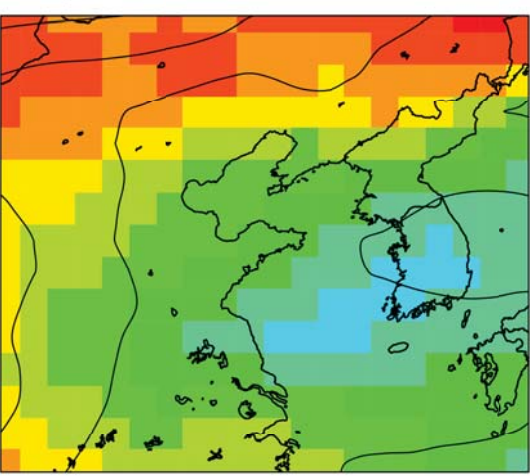
Figure 12.

Spread

Phase 1

Phase 2

Phase 3



Increment

Phase 1

Phase 2

Phase 3

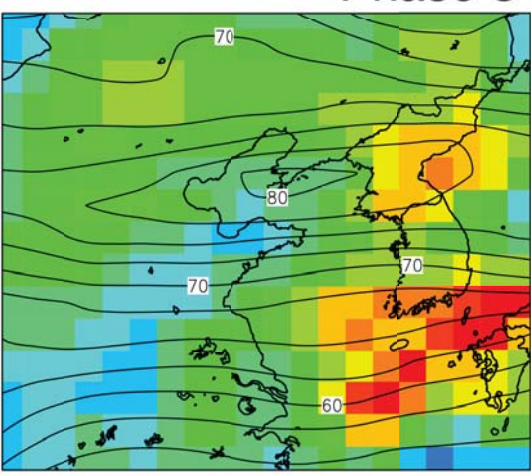
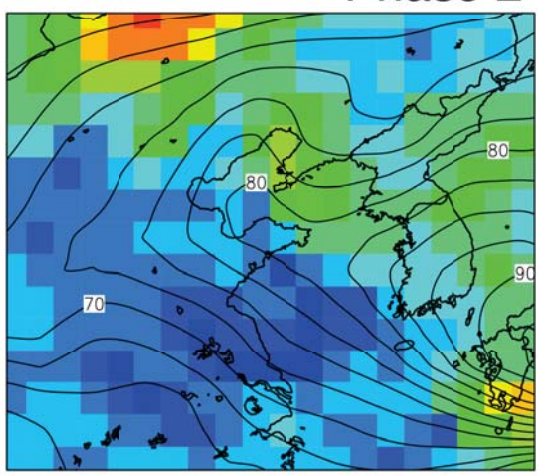
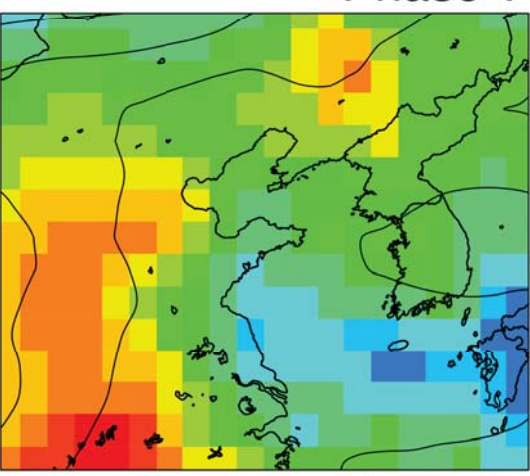


Figure 13.

Ozone bias relative to DC-8 (ppb)

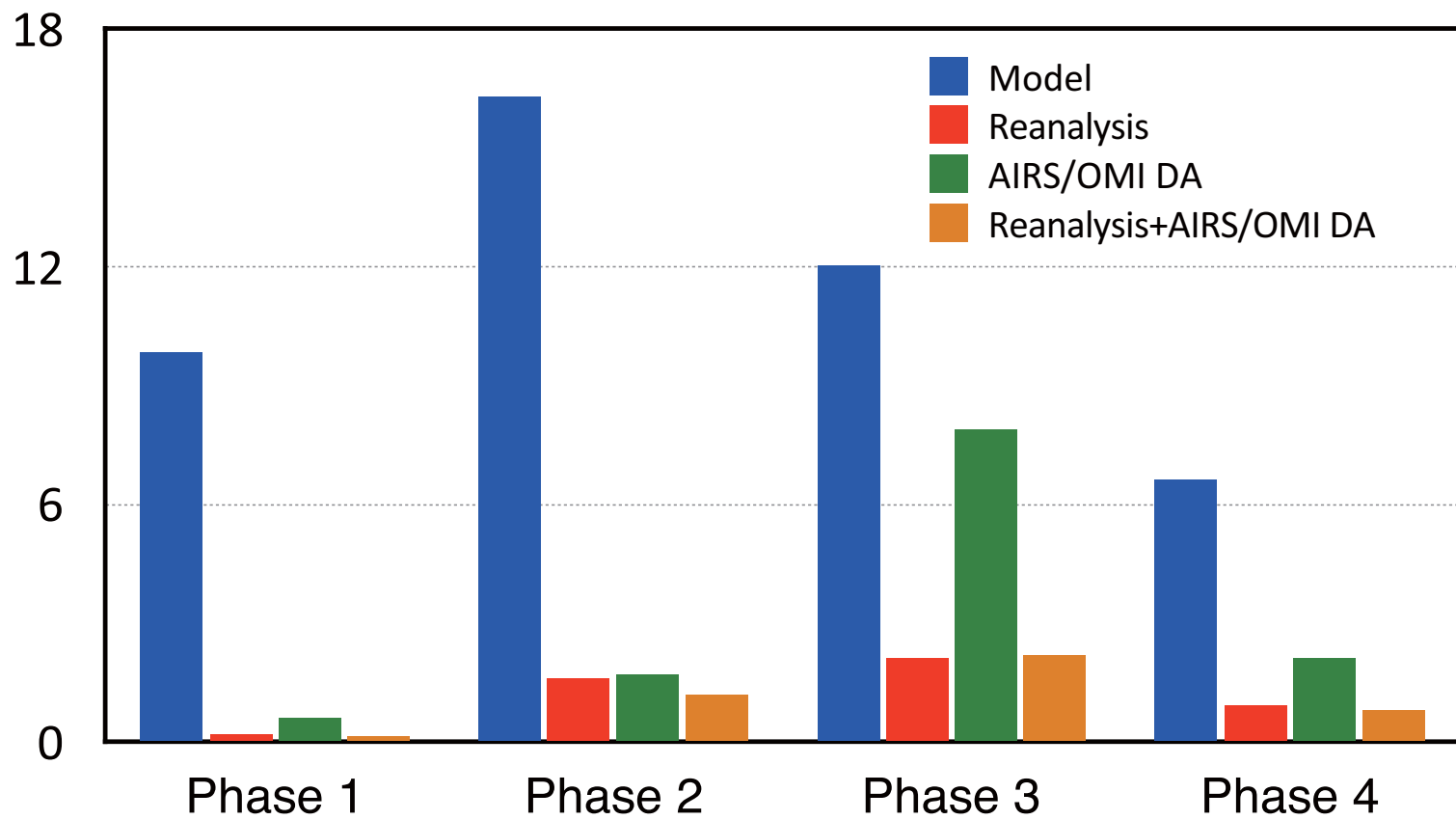
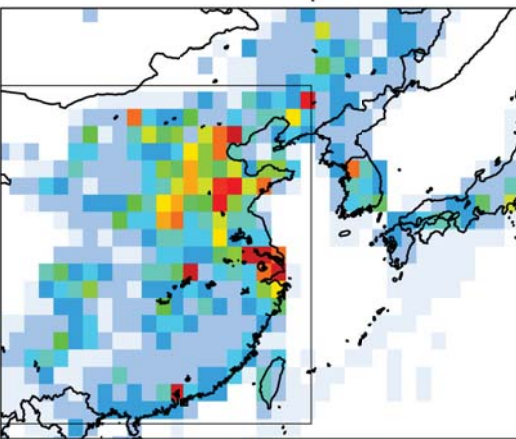
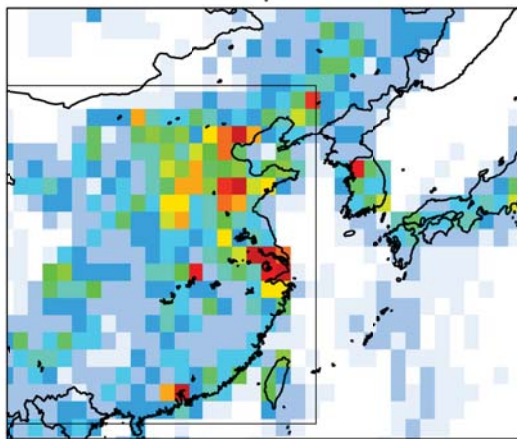


Figure 14.

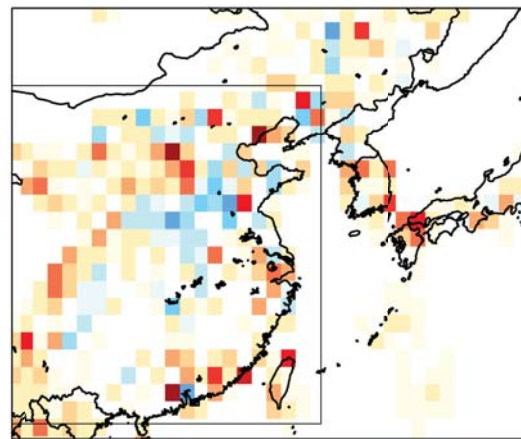
NO_x : A priori



NO_x : A posteriori



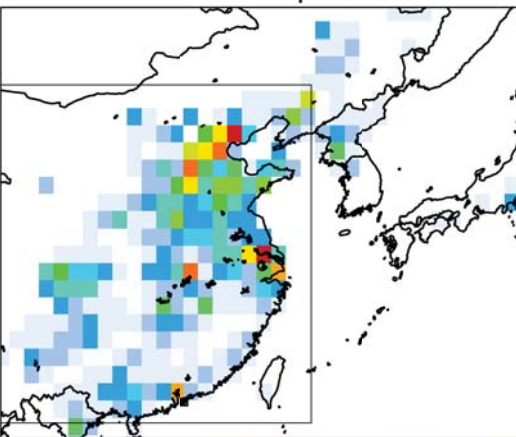
NO_x : Increment



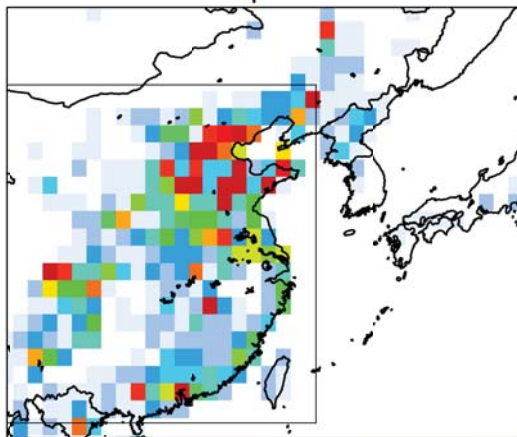
0.4 1 3 5 7 9 11 13 15 17 19 21 23 25 27

-8 -7 -6 -5 -4 -3 -2 -1 -0.5 0.5 1 2 3 4 5 6 7 8

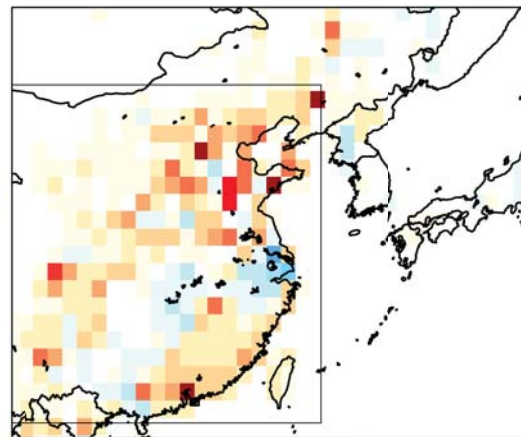
CO : A priori



CO : A posteriori



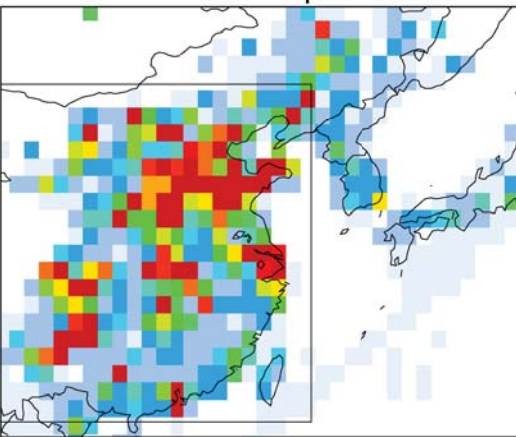
CO : Increment



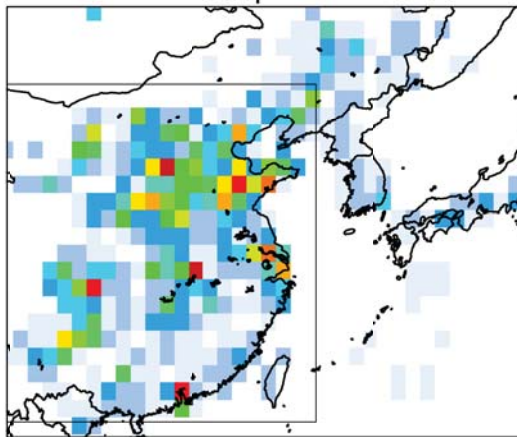
0.4 0.8 1.2 1.6 2 2.4 2.8 3.2 3.6 4 4.4 4.8 5.2 5.6 6

-7 -6 -5 -4 -3 -2 -1 -0.5 -0.1 0.1 0.5 1 2 3 4 5 6 7

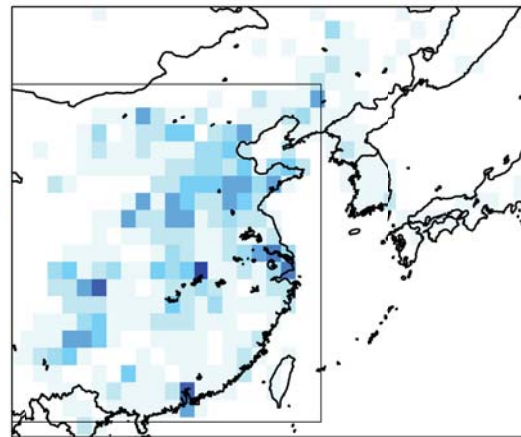
SO₂ : A priori



SO₂ : A posteriori



SO₂ : Increment



0.4 1 2.5 4 5.5 7 8.5 10 11.5 13 14.5 16 17.5 19 20.5

-6 -5 -4 -3 -2 -1.5 -1 -0.5 -0.1 0.1 0.5 1 1.5 2 3 4 5 6

Table 1. Mean values and standard deviations of ozone concentrations (in ppbv) based on data assimilation analyses averaged over the entire KORUS-AQ period and during individual phases. The results corresponding to the SMA, the KORUS-AQ domain (defined as 31.5°N–37.5°N, 123°E–132°E), and the East Asia domain (defined as 29°N–45°N, 110°E–132°E) using the DC-8 aircraft sampling and complete sampling 8-h daytime (9am to 5pm) mean chemical reanalysis fields at 700 hPa are shown.

	All period	Phase 1	Phase 2	Phase 3	Phase 4
SMA (aircraft)	76.7±9.4	75.0±13.7	78.9±5.9	77.3±8.0	75.5±2.9
SMA (complete)	75.1±7.6	73.1±5.3	79.8±4.1	77.7±6.2	77.1±7.8
KORUS-AQ area (aircraft)	75.8±5.3	74.6±6.5	77.7±6.2	76.0±4.3	73.9±2.9
KORUS-AQ area (complete)	70.5±9.2	70.4±7.2	75.5±6.6	70.0±8.7	72.4±8.3
East Asia (complete)	70.2±9.3	69.6±7.2	72.0±6.6	68.7±8.9	73.4±8.4

Table 2. Comparisons of mean ozone concentrations between the model simulation (Model), the standard data assimilation calculation (Reanalysis), and AIRS/OMI only data assimilation calculation (AIRS/OMI DA) in May 2016. Shown are the mean bias (BIAS: the data assimilation minus the satellite retrievals) and the root-mean-square error (RMSE) in ppbv. From left to right, results are shown for SH mid-latitudes (15–55°S), tropics (15°S–15°N), NH mid-latitudes (15–55°N) for the global product (GL), and for the East Asia regional product (RE).

		GL SH: 55 -15°S		GL TR: 15°S-15°N		GL NH: 15-55°N		RE	
		BIAS	RMSE	BIAS	RMSE	BIAS	RMSE	BIAS	RMSE
316 hPa	Model	14.3	20.1	-2.8	8.3	13.5	27.6	6.7	26.0
	Reanalysis	6.7	9.9	5.7	8.7	4.4	17.9	0.2	19.8
	AIRS/OMI DA	-0.2	7.6	-1.7	5.5	-3.3	15.8	-2.5	15.7
510 hPa	Model	4.0	8.3	-12.2	14.4	-1.3	12.0	-5.2	14.5
	Reanalysis	3.9	6.0	-1.8	6.6	3.9	9.2	0.9	10.5
	AIRS/OMI DA	0.1	3.7	-5.3	7.2	0.3	7.7	0.1	8.3
750 hPa	Model	0.3	4.3	-10.5	12.0	-3.0	8.2	-2.0	7.6
	Reanalysis	2.2	3.7	-3.1	6.0	3.9	7.6	4.8	6.8
	AIRS/OMI DA	0.3	2.8	-3.2	5.9	1.7	6.6	3.5	6.5

Table 3. Regional total surface emissions of NO_x (in Tg N yr⁻¹), CO emissions (in Tg CO yr⁻¹), and SO₂ (Tg SO₂ yr⁻¹) from a priori and a posteriori emissions for South Korea (125–129.5°E, 34.2–38.2°N) and eastern China (100–124°E, 21–43°N) in May 2016. The a posteriori NO_x emissions were derived using two different satellite NO₂ retrievals (QA4ECV and DOMINO2) in this study. The standard deviations of the estimated daily emissions during the analysis period are shown as the uncertainty information of the a posteriori emissions. The top-down estimates from the GlobEmission systems are also shown for NO_x and SO₂ emissions.

	South Korea			Eastern China		
	NO _x	CO	SO ₂	NO _x	CO	SO ₂
HTAP v2 2010	0.30	0.6	0.12	7.6	194.6	12.8
EDGAR v4.3.2 2012	0.43	2.6	0.8	8.2	107.5	29.8
KORUS v2	0.30	0.9	0.26	-	-	-
Top-down (QA4ECV)	0.42±0.05	1.1±0.2	0.07±0.02	8.3±0.3	231.3±10.0	4.5±1.1
Top-down (DOMINO2)	0.39±0.05	-	-	8.0±0.4	-	-
GlobEmission	0.37			6.2		20.9